Alma Mater Studiorum - Università di Bologna

Scuola di ingegneria e architettura

Corso di laurea in ingegneria chimica e di processo

Tesi di laurea magistrale

in

Dinamica e controllo dei processi chimici

EKF based State Estimation in a CFI Copolymerization Reactor including Polymer Quality Information

Candidato:
Filippo Tamagnini

Relatore:
Prof. Ferruccio Doghieri
Correlatore:
Prof. Sebastian Engell

Anno accademico: 2018/2019

Sessione III

Abstract

State estimation is an integral part of modern control techniques, as it allows to characterize the state information of complex plants based on a limited number of measurements and the knowledge of the process model. The benefit is twofold: on one hand it has the potential to rationalize the number of measurements required to monitor the plant, thus reducing costs, on the other hand it enables to extract information about variables that have an effect on the system but would otherwise be inaccessible to direct measurement.

The scope of this thesis is to design a state estimator for a tubular copolymerization reactor, with the aim to provide the full state information of the plant and to characterize the quality of the product.

Due to the fact that, with the existing set of measurements, only a small number of state variables can be observed, a new differential pressure sensor is installed in the plant to provide the missing information, and a model for the pressure measurement is developed.

Following, the state estimation problem is approached rigorously and a comprehensive method for analyzing, tuning and implementing the state estimator is assembled from scientific literature, using a variety of tools from graph theory, linear observability theory and matrix algebra. Data reduction and visualization techniques are also employed to make sense of high dimensional information.

The proposed method is then tested in simulations to assess the effect of the tuning parameters and measured set on the estimator performance during initialization and in case of estimation with plant-model mismatch.

Finally, the state estimator is tested with plant data.

Acknowledgements

This thesis was written during an ERASMUS exchange period in Germany at the Process Dynamics and Operations group in Technische Universität Dortmund. I'm truly grateful to the people in Bologna who coordinated this exchange (prof. Bonvicini and prof. Doghieri) and to my supervisors in Dortmund, Robin and Alexandru, for making everything work seemlessly, despite my best efforts to miss every possible deadline.

I want to thank Kirsten for lending me her bike and sending me in a quest to fetch the keys of the apartment in Gardenkamp, the first day of the exchange. I couldn't have thought of a better welcome and will probably remember it forever.

Thanks to Pourya, Egidio, Maximilian, Fabian, Clemens, Sankaranarayanan and all the other researchers in the DYN group for being such amazing people. Thanks also to my office mates Ramy, Jan, Tommaso and Markus, for the coffee breaks and the time spent together in the Gluteus Maximus bunker. Thanks to Pedro and Alexander for being the best possible flatmates.

Thanks to Penn Jillette for telling the best version of the aristocrats joke. Thanks to my friends and girlfriend for listening to my own version of the aristocrats joke, several times, helping me to perfect it and partly retaining friendship after each iteration.

Thanks to the European Union, its founders and partecipants for making this kind of experience possible. Meeting people from all over Europe (but also Egypt, Turkey, Iran, Lebanon, China, India, Russia, south America, etc...) gave me a sense of unity that will never fade away.

Finally, thanks to my family for accompanying me into adulthood.

It was a blast.

Contents

Nomenclature

Abbreviations

Entry	Meaning
AAM	Acrylamide monomer
AMPS	2-acrylamido-2-methylpropane sulfonic acid
CFI	Coiled flow inverter
EKF	Extended Kalman filter
HPLC	High pressure liquid chromatoghraphy
KPS	Potassium persulfate
MPC	Model predictive control
NaFS	Sodium formaldehyde sulfoxylate
NACL	Number average chain length
NMPC	Nonlinear model predictive control
PDI	Polydispersity index
PTFE	Polytetrafluoroethylene
SVD	Singular value decomposition
WACL	Weight average chain length

Latin symbols

Symbol	Meaning as scalar or vector	Meaning as matrix
A	Area	Dynamic matrix
B		Input matrix
c_s	Concentration of the specie s	
C_p		Parameter covariance matrix
C_P	Heat capacity	
D_{ax}	Axial dispersion coefficient	
D_i	Dead chain moments	
D	Diameter	
e	Error or Napier's constant	Exponential matrix
E	Expected value	
E_r	Activation energy for the reaction r	
f	Dynamic function	
F	Volume flowrate	State transition matrix
F_w	Mass flowrate	
g	Gravitational acceleration	
G		Discrete input matrix
h	Measurement function	
H	Enthalpy	Jacobian of h with respect to the state
I	Intensity spectrum	Identity matrix
$J_{f,p}$		Jacobian of f with respect to p
k	Constant	
k_M	Tuning parameter for the matrix M	
k_r	Kinetic constant for the reaction r	
K	Power law viscosity coefficient	Kalman gain
L	Length	
m	Measurement noise	
M_s	Molar mass of the specie s	
n	Power law exponent	
$\dot{n}$	Molar flowrate	
N	Number	
p	Parameter vector	

Symbol	Meaning as scalar or vector	Meaning as matrix
P	Pressure	Covariance matrix
P_{ij}	$j-$th moment of the polymer chain i	
Q		Process noise covariance matrix
$\dot{Q}$		Continuous-time Q
Q_j	$j-$th moment of the polymer chains	
r	Radial coordinate	
r_k	Residual at time k	
R	Radius or ideal gas constant	Measurement noise covariance matrix
t	Time	
T	Temperature	
u	Controlled input vector	
U	Overall heat transfer coefficient	
v	Velocity	
v_i	Eigenvector	
w	Process noise vector	
x	State vector	
X		State matrix or state sample matrix
y	Measurement vector	
Y		Output sample matrix
z	Axial position	

Greek symbols

Symbol	Meaning as scalar or vector
α	Residual index
$\dot{\gamma}$	Strain rate
Γ	Raman calibration matrix
δ	Deviation
Δ	Difference
ϵ	Tolerance
η	Viscosity
λ	Heat conductivity
λ_i	Eigenvalue
Λ	Relaxation time
μ	Moment (of a distribution)
ρ	Density
σ	Singular value
Σ	Measurement noise standard deviation matrix
τ	Shear stress
ϕ	Distribution
ψ_i^2	Unobservability index
Ψ	Observability matrix residual
ω	Mass fraction

Subscripts

Symbol	Meaning
atm	Atmospheric
ax	Axial
c	Corrected, clipped
f	Fluid, fluid-side, function
i	State index or generic index
j	State index or generic index, jacket
k	Time instance
m	measured
n	Negative
p	Parameter
q	Cross section
r	Reactor, fluid
s	Sampling, sensor, simulation, states
sc	Scaling
ss	Steady state
t	Tube, tube-side
u	Complementary
0	Initial, characteristic, zero limit
∞	Infinite-time or temperature

Calligraphic symbols

Symbol	Meaning
$\mathbb{A}$	Set
$\mathcal{D}$	Diffusivity
$\mathcal{N}$	Normal distribution
$\mathcal{O}$	Kalman observability matrix
$\mathcal{R}$	Generative (reaction) term
$\mathbb{R}$	Real numbers
$\mathcal{S}$	Structural observability matrix

Dimensionless numbers

Symbol	Meaning
Bo	Bodenstein number
Gz	Graetz number
Nu	Nusselt number
Pr	Prandtl number
Re	Reynolds number
Sc	Schmidt number

Chapter 1

Introduction

Nowadays, major efforts are being made in the chemical industry to shift processes from batch to continuous operation. There are several motivations for this endeavour, such as the aim to increase productivity: continuous processes are generally capable of producing higher quantities of product per unit time and volume than their batch counterparts, not to mention the ability to rationalize resource usage and to achieve more consistent product quality over time.

Some processes, such as polymerizations, are still operated in batch nonetheless, owing to the to difficulties that originate from the high viscosities of the fluid systems in place and the complex behaviour of the reaction systems. Polymeric fluids pose significant challenges when it comes to heat exchange and mixing inside tubular reactors, and the loss of control on temperature can trigger polymerization runaways and loss of operability of the reactor, as it is illustrated in the events diagram in figure 1.1. On the other hand, it makes very little sense to operate polymerizations in continuous stirred tank reactors (CSTR), as the very broad residence time distribution of such reactors would result in relatively low conversions of the feedstock and poor product quality.

Novel reactor concepts and modern control techniques can be used to overcome such difficulties. This thesis' work is framed inside a project to develop a reactor technology for transferring the production of sulfonated polyacrylamide from batch to continuous processing by the means of a coiled flow inverter (CFI) reactor. Prior contributions to this project are discussed in [42, 9, 26, 23, 49, 27].

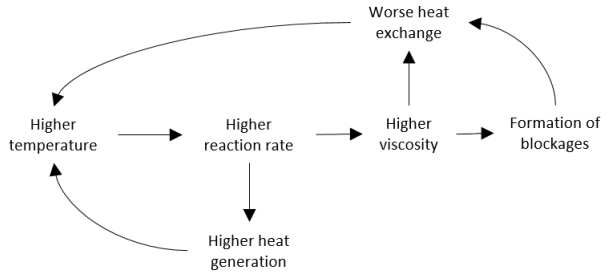

Figure 1.1: Polymerization runaway mechanism

In order to tackle the difficult control problem that arises from the inherent delay behaviour of tubular reactors, nonlinear model predictive control (NMPC) was identified as a viable solution to operate the reactor (at least for high level control), together with a model based state observer to reconstruct as much information as possible about the state of the reactor from a limited number of measurements.

The reactor was equipped in previous works with temperature sensors [42] and one Raman spectrometer [9], that were found to be insufficient for the observer to reconstruct the full information of the plant. The main objective of this thesis is to extend the capabilities of the observer by installing a pressure drop sensor at the outlet of the reactor and integrating the new measurement in the estimation scheme.

To do so, the pressure drop in the outlet piping of the reactor has to be modelled, as well as the correlation between the composition of the mixture and the properties of the fluid. Simple models exist to describe the rheological behaviour of polymeric mixtures in the limit of low concentrations, such as the Mark-Houwink equation [39], however the ambition of this work is to propose a more descriptive model that is flexible enough to describe the behaviour of the concentrated polymer.

Once the model has been developed, the measurement has to be integrated in the state observer, the observability of the system characterized and the state observer tuned accordingly. To do this, the state estimation problem is approached rigorously and several tools are selected from scientific literature and put to the test in simulations and with real data from the plant.

Chapter 2

Theoretical background

2.1 Polymer systems

Polymers are macromolecules constituted by a number of smaller molecules, called monomers, linked together to form long chains. The reactions leading to the formation of such molecules are called polymerization reactions. Polymers constituted by two or more different monomers are called copolymers, and if the sequence of monomers does not follow any particular pattern they are further specialized as random copolymers [33].

2.1.1 Polymerization reactions

Polymers can form according to different mechanisms, such as polyaddition or polycondensation, step or chain polymerizations. In polyaddition reactions, the structure of the monomeric units is preserved in the polymer chains and the molecular weight of the polymer is the sum of the molecular weights of the monomers. [33].

In chain polymerizations the growth of chains occurs in specific reactive centers that originate in the initiation step, in radical, acid/base or photochemical reactions and propagate along the chain as new monomers are incorporated. If two reactive centers meet, the reaction terminates (either by coupling or disproportionation) [33].

The Acrylamide - AMPS copolymerization process is described by four groups of reactions: initiation, polymer propagation, termination and inhibition [42].

In this section the letter Q is used in reference to the polymer molecules, and in particular $Q^{\bullet}_{i,n}$ is to be intended as the polymer chain of length n and active (terminal) monomer i. $Q_{D,n}$ indicates the inactive (dead) polymer chain of length n.

The two monomers are acrylamide monomer (AAM) and 2-acrylamido-2-methylpropane sulfonic acid (AMPS).

Initiation

The first step in the reaction is the decomposition of the initiator in active radicals:

$$\mathrm{Ini} \xrightarrow{k_d f} 2\mathrm{R}^{\bullet} \tag{2.1.1}$$

The kinetic constant k_d is multiplied by a radical efficiency factor f that accounts for the parallel reactions of the initiator that don't result in the formation of active radicals.

The chemicals used as initiators are potassium persulfate (KPS) and sodium formaldehyde sulfoxylate (NaFS), with KPS being the limiting reactant.

Once the radical is formed, it can react with the monomers to create live polymer chains:

$$\mathrm{R}^{\bullet} + \mathrm{M}_1 \xrightarrow{k_{ini,1}} \mathrm{Q}^{\bullet}_{1,1} \tag{2.1.2}$$

$$\mathrm{R}^{\bullet} + \mathrm{M}_2 \xrightarrow{k_{ini,2}} \mathrm{Q}^{\bullet}_{2,1} \tag{2.1.3}$$

Polymer propagation

The second step in the reaction is the propagation of the active polymer chains:

$$\mathrm{Q}^{\bullet}_{1,n} + \mathrm{M}_1 \xrightarrow{k_{p,11}} \mathrm{Q}^{\bullet}_{1,n+1} \tag{2.1.4}$$

$$\mathrm{Q}^{\bullet}_{1,n} + \mathrm{M}_2 \xrightarrow{k_{p,12}} \mathrm{Q}^{\bullet}_{2,n+1} \tag{2.1.5}$$

$$\mathrm{Q}^{\bullet}_{2,n} + \mathrm{M}_1 \xrightarrow{k_{p,21}} \mathrm{Q}^{\bullet}_{1,n+1} \tag{2.1.6}$$

$$\mathrm{Q}^{\bullet}_{2,n} + \mathrm{M}_2 \xrightarrow{k_{p,22}} \mathrm{Q}^{\bullet}_{2,n+1} \tag{2.1.7}$$

The polymer growth mechanism is chain polymerization (meaning that the polymer chains grow by one monomeric unit at a time).

Termination

The final step in the polymerization reaction is the termination by combination or disproportionation:

$$\mathrm{Q}^{\bullet}_{i,n} + \mathrm{Q}^{\bullet}_{j,m} \xrightarrow{k_{tc,ij}} \mathrm{Q}_{D,n+m} \tag{2.1.8}$$

$$\mathrm{Q}^{\bullet}_{i,n} + \mathrm{Q}^{\bullet}_{j,m} \xrightarrow{k_{td,ij}} \mathrm{Q}_{D,n} + \mathrm{Q}_{D,m} \tag{2.1.9}$$

Inhibition

In addition to the two termination mechanisms cited above, the chain growth can be stopped (or inhibited) by the presence of an additional component, such as dissolved oxygen, that reacts with active radicals and generates inactive peroxy radicals, peroxides and hydroperoxides [42]:

$$\mathrm{R}^{\bullet} + \mathrm{O}_2 \xrightarrow{k_{inh}} \mathrm{R} \tag{2.1.10}$$

$$\mathrm{Q}^{\bullet}_{i,n} + \mathrm{O}_2 \xrightarrow{k_{inh}} \mathrm{Q}_{D,n} \tag{2.1.11}$$

2.1.2 Polymer distribution

One of the main challenges in describing a polymer system comes from the fact that such system is composed of an unspecified number of polymer chains of different chain lengths. On one hand the macroscopic properties of a polymer mixture are determined by its distribution [39], on the other hand keeping track of all the possible configurations (in terms of chain lengths and composition) would be computationally expensive and ultimately uninformative for process control purposes.

One widely used technique to model polymeric mixtures makes use of the method of moments [32]. The n-th moment of a distribution ϕ is given as:

$$\mu_n = \sum_{k=1}^{\infty} k^n \cdot \phi_k \tag{2.1.12}$$

If we set ϕ as the distribution of molar concentrations of the polymer chains of length k, we can write the zeroth, the first and the second moment as:

$$Q_0 = \sum_{k=1}^{\infty} c_k \tag{2.1.13}$$

$$Q_1 = \sum_{k=1}^{\infty} k \cdot c_k \tag{2.1.14}$$

$$Q_2 = \sum_{k=1}^{\infty} k^2 \cdot c_k \tag{2.1.15}$$

The zeroth and first moment have a clear physical meaning in this context, Q_0 being the total molar concentration of the polymer and Q_1 the number of monomeric units incorporated in the polymer chains per unit volume.

Many properties of the polymer can be described by two indices: the number average chain length (NACL) and the weight average chain length (WACL).

$$\text{NACL} = \frac{Q_1}{Q_0} \tag{2.1.16}$$

$$\text{WACL} = \frac{Q_2}{Q_1} \tag{2.1.17}$$

The ratio between WACL and NACL is commonly referred to as polydispersity index (PDI), and gives a measure of the broadness of the distribution:

$$\text{PDI} = \frac{Q_2 \cdot Q_0}{Q_1^2} \tag{2.1.18}$$

A visual representation of a polymer distribution and its average chain lengths is provided in figure 2.1.

In the context of this work WACL is of particular interest due to its strong connection with the viscosity of the polymer [7].

With the approach 2.1.2 it is also possible to write the reaction kinetics and the

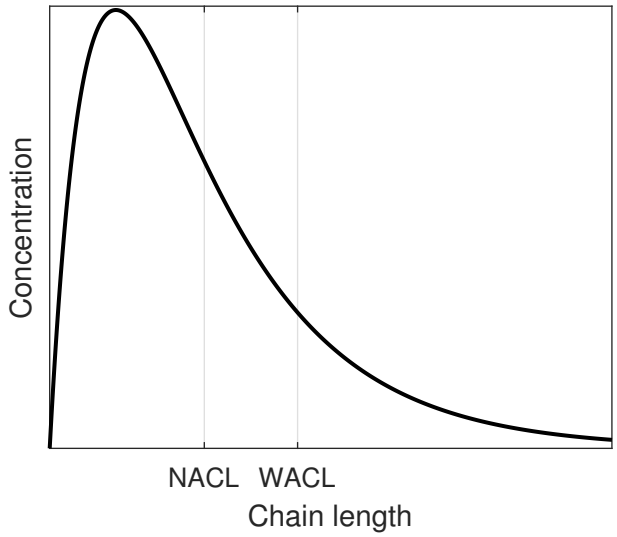

Figure 2.1: Example of a chain length distribution for a polymeric mixture

conservation equations in terms of the moments. This is extensively described in [32] for the general case and in [42] for the existing plant, to which reference should be made for a more detailed discussion. The main idea, however is to treat the individual moments as physical quantities, and to write their derivatives in terms of the derivatives of the elements in the distribution:

$$\frac{\partial \mu_n}{\partial t} = \sum_{k=1}^{\infty} k^n \cdot \frac{\partial \phi_k}{\partial t} \tag{2.1.19}$$

$$\frac{\partial \mu_n}{\partial z} = \sum_{k=1}^{\infty} k^n \cdot \frac{\partial \phi_k}{\partial z} \tag{2.1.20}$$

$$\frac{\partial^2 \mu_n}{\partial z^2} = \sum_{k=1}^{\infty} k^n \cdot \frac{\partial^2 \phi_k}{\partial z^2} \tag{2.1.21}$$

The derivatives of the individual elements of the distribution are typically linked to each other through conservation equations:

$$\frac{\partial \phi_k}{\partial t} = \mathcal{D} \cdot \frac{\partial^2 \phi_k}{\partial z^2} - v \cdot \frac{\partial \phi_k}{\partial z} + \mathcal{R}_k(\phi) \tag{2.1.22}$$

It is possible to apply the method of moments to conservation equations, and by replacing the summations with 2.1.19 to 2.1.21, equation 2.1.23 is derived:

$$\frac{\partial \mu_n}{\partial t} = \mathcal{D} \cdot \frac{\partial^2 \mu_n}{\partial z^2} - v \cdot \frac{\partial \mu_n}{\partial z} + \sum_{k=1}^{\infty} k^n \cdot \mathcal{R}_k(\phi) \tag{2.1.23}$$

The last step in the derivation of moment conservation equations requires to algebraically simplify the term

$$\sum_{k=1}^{\infty} k^n \cdot \mathcal{R}_k(\phi) \tag{2.1.24}$$

and to express it in terms of the moments. This is shown in [42, 32].

2.1.3 Polymer fluid dynamics

In order to correlate the properties of the polymer to the measured pressure drop, it is necessary to describe the fluid dynamic behaviour of the fluid inside the measurement apparatus.

Due to the size and elongated shape of the polymer chains, the intermolecular forces determine an overall complex effect on the fluid system and ultimately result in non-Newtonian behaviour [39, 7].

Newtonian fluids are among the simplest classes of fluids, with constant shear stress-strain rate relation (viscosity), memoryless behaviour and negligible normal stress-strain rate relation. Non-Newtonian fluids, on the other hand, exhibit nonlinear viscosity, persistence of stress after deformation and measurable normal stresses resulting from shear flows [7, 8].

Viscosity

Strain rate $\dot{\gamma}$ is the rate of change of velocity between surfaces parallel to the flow, and for monodimensional flow in pipes can be written as [7, 8]:

$$\dot{\gamma} = \frac{\partial v}{\partial r} \tag{2.1.25}$$

Shear stress τ is the frictional force per unit surface that parallel fluid fillets exhert on each other. For generalized Newtonian fluids it is possible to write [7, 8]:

$$\tau = -\eta(\dot{\gamma}) \cdot \dot{\gamma} \tag{2.1.26}$$

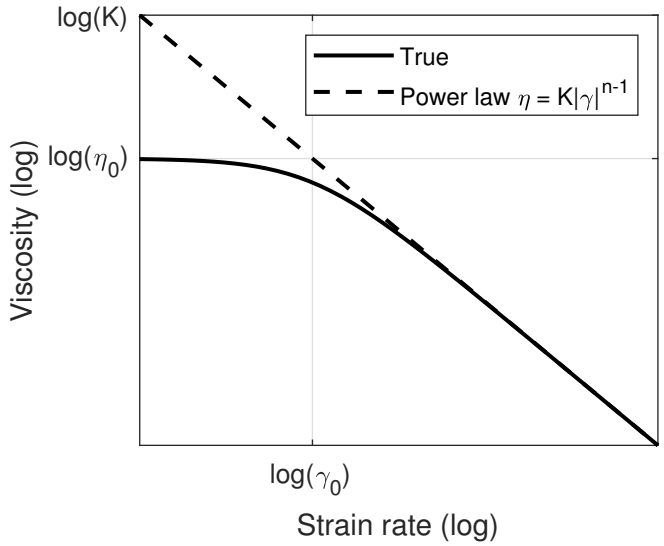

Figure 2.2: Comparison of the true viscosity in polymeric fluids and the power law approximation as a function of the strain rate [7]

For Newtonian fluids in isothermal flows η is constant. Viscosity in polymeric fluids in intermediate strain rates follows a power law instead [7, 8]:

$$\eta(\dot{\gamma}) = K \cdot |\dot{\gamma}|^{n-1} \tag{2.1.27}$$

with $n < 1$ (shear thinning fluid).

For very low strain rates, viscosity settles to some plateau value η_0 (zero strain rate viscosity). The strain rate around which the transition between one regime and the other occurs is called transition strain rate and is denoted as $\dot{\gamma}_0$ [7].

Polyacrylamide solutions are found to encounter a further change in regime for very high strain rates, at which the fluid becomes shear thickening [19]. This effect will be neglected due to the low velocities encountered in the plant.

An illustration of the transition between the Newtonian and the shear thinning regime is shown in figure 2.2, together with the power law model.

For concentrated polymer solutions, η_0 is usually found to be proportional to some power of the weight average chain length [7]:

$$\eta_0 \propto \mathrm{WACL}^{\alpha} \tag{2.1.28}$$

with

$$\alpha = \begin{cases} 1 & \text{WACL} < \text{CL}_c \\ 3.4 & \text{WACL} \geq \text{CL}_c \end{cases} \tag{2.1.29}$$

The value of CL_c (critical chain length) depends on the polymer weight concentration and is determined experimentally.

The transition strain rate also follows different regimes depending on the weight average chain length:

$$\dot{\gamma}_0 \propto \begin{cases} 1 & \text{WACL} < \text{CL}'_c \\ Q_2 & \text{WACL} \geq \text{CL}'_c \end{cases} \tag{2.1.30}$$

with CL'_c slightly larger than CL_c [7].

Viscosity is heavily affected by temperature. A simple model is given by the Andrade equation [3]:

$$\eta \propto e^{T_0/T} \tag{2.1.31}$$

Finally, the power law exponent n in equation 2.1.27 is a function of the moments as well and spans the range $[0.9, 0.2]$ when going from high dilution to concentrated solutions [7]. It is assumed that this parameter stays reasonably constant and near the lower limit when operating the reactor at steady state. This hypotesis is valid by means of literature [16, 19] but should be verified experimentally.

Elasticity

Memory effects are quantified by the Deborah number:

$$De = \frac{\Lambda}{t_c} \tag{2.1.32}$$

where Λ is the relaxation time of the polymer and t_c is a characteristic time for the flow. When $De << 1$, elastic effects are negligible. If, however, $De \sim 1$ or higher, the polymer will react lazily to changes in flowrate, resulting in residual stresses and therefore spurious pressure drop readings [7].

For concentrated polyacrilamide solutions, literature provides a relaxation time in the order of 1s [19]. This suggests an upper bound the for measurement

bandwidth between flowrate changes of about one sample per second, but does not require further modelling.

Normal stresses

Normal stresses resulting from shearing flow should be taken into account when mounting the differential pressure sensor, due to the hole pressure effect [30]. In practice, when measuring pressure in a pipe carrying a polymeric fluid, one will observe different readings depending on whether the pressure sensor is flush mounted or recessed with respect to the pipe wall, and in particular the latter measurement will be smaller than the former. If one is not interested in knowing the absolute pressure of the fluid inside the pipe but wants to perform a pressure drop measurement, he should still make sure that the fluid distance between the pipe wall and the pressure sensor is either the same for both terminals or enough to dissipate all normal stresses, in order to get a correct reading.

2.2 Coiled flow inverter

The Coiled Flow Inverter (CFI) is a modern reactor concept that allows for quasi-plug flow behaviour even at low values of the Reynolds number and in laminar flow [25].

The CFI reactor exploits two fluid dynamics phoenomena: Dean vortices that arise when a fluid moves through a coil [11] and rotation of such vortices (inversion) in bends [25].

The geometry of the reactor and its flow patterns are illustrated in figure 2.3. The reactor pipe is coiled around a rod that provides structural support. During flow, the difference in distance from the coil axis imparts a secondary flow pattern to the fluid that is parallel to the pipe section. The vortices that result from this motion significantly improve radial mixing [31].

After a number of coils, a bend is made and the orientation of the secondary flow switched. This is what is referred to as inversion. The effect of flow inversion is to “scramble” the fluid and to shift elements that lied before on higher residence time streamlines to faster moving regions. The overall effect is to narrow the residence time distribution [37, 38, 40].

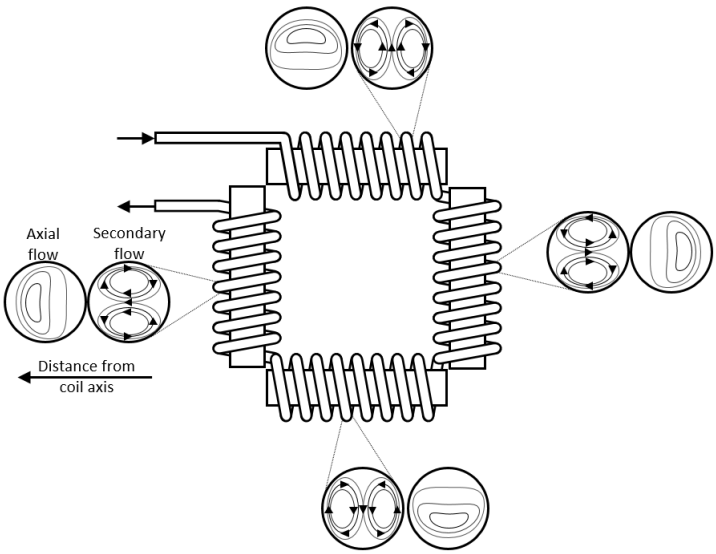

Figure 2.3: CFI geometry and flow patterns [25]

2.3 Model predictive control

Model Predictive Control (MPC) is a control philosophy that made its debut in industry during the seventies for linear systems, but only recently started to gain momentum in its nonlinear applications (NMPC), due to the decrease in cost for computing power and the availability of commercial software frameworks [10]. As the name suggests, MPC is a model based technique, therefore a good model of the process is required for it to be used. A certain amount of model uncertainty can be tolerated by robust MPC techniques [10, 36].

The main idea behind MPC is to compute a sequence of inputs for the plant to bring it from an initial operating point to another in the best way possible. The optimality of the path is determined by a cost function that accounts for the time required for reaching the objective and the effort of the controller [10, 36].

Compared to classical control, MPC is capable of handling multivariable nonlinear systems and constraints in a very natural way, thus enabling very tight control even in strongly coupled processes. Moreover, the optimality of the control input can translate in quicker reaction to changes in set-point and lower operating costs of the process [10, 36].

The price to pay for setting up such a control system is a higher initial cost

for the determination of a suitable model and the availability of full state information about the system[10, 36].

The NMPC implementation for the plant is made in Python using the open source software do-mpc and CasADi.

do-mpc (Dortmund model predictive control) [28] is a modular environment for the implementation of NMPC that was developed in Technische Universität Dortmund. The modularity allows for fast prototyping and transition from simulation to online applications, and is used in this work as a platform for simulations.

CasADi [2] is an open source symbolic framework for automatic differentiation and numerical optimization. It allows to write models in terms of symbolic variables and to automatically compute the exact derivatives, as opposed to using the less precise and more expensive finite differences methods.

The model of the plant is written using CasADi, and most of the computations (integration of differential equations, calculation of gradients, model function evaluations) are done within its environment.

2.4 State estimation

As it was stated before, one of the requirements of MPC is the availability of full state information about the process. This could in theory be accomplished by installing as many sensors as the state variables, but in practice it would be expensive if not impossible at all: some variables can only be measured offline, others could be physically not accessible. One appealing possibility is to infer the state information from a limited number of measured variables and the knowledge about the process. A device that accomplishes this task is called state observer or state estimator [44].

2.4.1 State space representation of dynamical systems

Continuous-time systems

The evolution in time of a continuous-time system can be described by the set of differential equations:

$$\dot{x} = f(x, u) \tag{2.4.1}$$

where f is a generic nonlinear function of the state vector x and the controlled input vector u.

If f is linear, then it is possible to write the system as:

$$\dot{x} = Ax + Bu \tag{2.4.2}$$

where A and B are matrices of appropriate sizes.

A nonlinear system can be linearized around the state x_0 and input u_0 by approximating equation 2.4.1 in a truncated Taylor series [43]:

$$\dot{x} \simeq f(x_0, u_0) + A(x - x_0) + B(u - u_0) \tag{2.4.3}$$

with A, B the jacobians of f with respect to x and u, respectively:

$$A_{ij} = \left(\frac{\partial f_i}{\partial x_j}\right)_{x_0,u_0} \tag{2.4.4}$$

$$B_{ij} = \left(\frac{\partial f_i}{\partial u_j}\right)_{x_0,u_0} \tag{2.4.5}$$

Discrete-time systems

If the state of the system is only considered in discrete instants of time t_k, the system is said to be discrete-time. Discrite-time systems arise, for example, when measurements from a continuous time system are sampled and fed to a digital computer.

It is possible to write the evolution of a discretized nonlinear continuous-time system in terms of the solution $x(t_{k+1})$ of the initial value problem:

$$\begin{cases} \dot{x} & = f(x, u) \\ x(t_k) & = x_k \end{cases} \tag{2.4.6}$$

Linear discrete-time systems are described by:

$$x_{k+1} = Fx_k + Gu_k \tag{2.4.7}$$

where F is called transition matrix.

It is possible to transform a continuous-time linear system into a discrete-time linear system under the assumption of constant $u(t)$, A and B during the sampling period by transforming the A and B matrices as follows [34]:

$$F = e^{At_s} \tag{2.4.8}$$

$$G = \left(\int_0^{t_s} e^{At} dt \right) B \tag{2.4.9}$$

A nonlinear system can be rigorously discretized and linearized under the assumption of constant $u(t)$ during the sampling period by setting F and G as the jacobians:

$$F_{i,j} = \left(\frac{\partial \hat{x}_{k,i}^-}{\partial \hat{x}_{k-1,j}} \right)_{x_{k-1}, u_{k-1}} \tag{2.4.10}$$

$$G_{i,j} = \left(\frac{\partial \hat{x}_{k,i}^-}{\partial \hat{u}_{k-1,j}} \right)_{x_{k-1}, u_{k-1}} \tag{2.4.11}$$

Measurement function

The description of the system is completed by defining the measured vector y_k and the measurement function:

$$y_k = h(x_{k,} u_k) \tag{2.4.12}$$

The measurement function can be linearized around a certain state x_0 just as it was done with the dynamics equation:

$$y_k \simeq h(x_0, u_0) + H(x_k - x_0) \tag{2.4.13}$$

with H the jacobian of h with respect to x:

$$H_{ij} = \left(\frac{\partial h_i}{\partial x_j} \right)_{x_0, u_0} \tag{2.4.14}$$

Distributed parameter systems

The expressions presented so far are only valid for a restricted class of systems (concentrated parameter systems) and are typically the result of some simplifications. Physical systems of interest for chemical engineers are seldom governed by ordinary differential equations and require some treatment before proceeding any further.

The state in distributed parameter systems is a function of both time and the position in space. A description of the system can be made in terms of partial derivatives, such as the convection-diffusion equation [8]:

$$\frac{\partial c}{\partial t} = \mathcal{D} \cdot \frac{\partial^2 c}{\partial z^2} - v \cdot \frac{\partial c}{\partial z} + \mathcal{R} \tag{2.4.15}$$

with c a state variable (such as the concentration of one reactant or the temperature), v the fluid velocity in the spatial direction z, $\mathcal{D}$ a dispersion coefficient and $\mathcal{R}$ a generative term.

Distributed parameter systems can be approximated by systems of ordinary differential equations by discretizing the spatial derivatives in selected grid points, using techniques such as the finite differences method [18].

2.4.2 Stability

There exist a large number of definitions for stability. Broadly speaking a system (discrete-time or continuous-time) is said to be stable if, for any initial state that is close to a steady state, the trajectory of the system remains close to the steady state. If the trajectory of the system asymptotically converges towards the steady state, the system is said to be asymptotically stable.

For linear systems, simple criteria can be used to assess stability, while for nonlinear system multiple steady states can exist with domains of attraction surrounding each stable steady state [24]. It is possible to linearize nonlinear systems around steady states and test stability in the direct vicinity.

Asymptotic stability criterion

A discrete-time linear system described by $x_{k+1} = Fx_k$ is asymptotically stable if all of the eigenvalues λ_i of $F \in \mathbb{R}^{n \times n}$ have magnitudes smaller than one [44].

Furthermore, the eigenvectors v_i that satisfy

$$\lambda_i v_i = F v_i \tag{2.4.16}$$

are called modes of the system.

2.4.3 Observability

A discrete-time system is said to be observable if, for any initial state x_0 and any final time t_k, the initial state x_0 can be uniquely determined by the knowledge of the input u_j and output y_j for all $j \in [0, k]$ [44].

Criteria exist for checking observability in linear systems, while for nonlinear systems there are no simple tests and the previous statement has to be demonstrated for the particular case. One possibility is to use linear observability criteria on the linearized system to evaluate local observability [44].

Two common tests for observability are the Kalman observability criterion [22] and the Hautus observability criterion [17]. The former test is the most straightforward to implement, however is numerically unstable for systems of considerable size [35] and is generally used only for didactic purposes, while the latter is slightly more robust but requires an eigenvalue computation.

A necessary condition for observability in tubular reactors reactors is proposed in [13].

Kalman observability criterion

A discrete-time linear system is observabile if the observability matrix:

$$\mathcal{O} = \begin{pmatrix} H \\ HF \\ HF^2 \\ \cdots \\ HF^{n-1} \end{pmatrix} \tag{2.4.17}$$

has full rank, with n = number of states [22].

The Kalman observability criterion can be expressed for continuous-time systems by replacing F with A.

Algorithm 2.1 Computation of the unobservability indices [21]

1. Compute $\mathcal{O}^+$ as the Moore-Penrose inverse of $\mathcal{O}$ (see section C.2).
2. Compute $\Psi = [\Psi_1, \Psi_2, \ldots, \Psi_n]^T$ as

$$\Psi = I - \mathcal{O}^+\mathcal{O} \tag{2.4.19}$$

3. Compute the unobservability indices vector ψ^2 as

$$\psi_i^2 = \|\Psi_i\|_2^2 \tag{2.4.20}$$

Hautus observability criterion

A discrete-time linear system (F, H) is observable if the matrix

$$\begin{pmatrix} \lambda_i I - F \\ H \end{pmatrix} \tag{2.4.18}$$

has full rank for every λ_i eigenvalue of F [17]. The eigenvectors for which the test fails are called unobservable modes of the system.

The Hautus observability criterion can be expressed for continuous-time systems by replacing F with A.

Method of the unobservability indices

Once the matrix $\mathcal{O}$ has been calculated, it is possible to identify the contribution of individual states to unobservability by computing their unobservability indices. The procedure is demonstrated in [21] and is illustrated in algorithm 2.1:

Fully observable states are characterized by $\psi_i^2 = 0$, while unobservable ones are those such that $\psi_i^2 > 0$. Additionally, it can be proven that [21]:

$$n - rank(\mathcal{O}) = \sum_{i=0}^{n} \psi_i^2 \tag{2.4.21}$$

Let x_0 be the initial state of the system and y_k the measurement at time k.

Let $Y = \begin{pmatrix} y_0^T & y_1^T & \dots & y_k^T \end{pmatrix}^T$:

$$Y = \begin{pmatrix} H \\ HF \\ \vdots \\ HF^{n-1} \end{pmatrix} x_0 = \mathcal{O} x_0 \tag{2.4.22}$$

If $\mathcal{O}$ is not full rank[1], it is possible to write:

$$x_0 = \mathcal{O}^+ Y + \left(I - \mathcal{O}^+ \mathcal{O}\right) z \tag{2.4.23}$$

where $z \in \mathbb{R}^{n \times 1}$ is an arbitrary vector and $\left(I - \mathcal{O}^+ \mathcal{O}\right) z$ the free solution. States with an unobservability index greater than zero have a nonzero weight on the free solution, meaning that their initial state cannot be determined uniquely [21].

Moreover, when state estimation is applied on processes with noise, the tolerance used in computing the pseudoinverse (see appendix C.2) can be set higher to distinguish between observable and unobservable states in relation to the measurement noise [21].

Structural observability in tubular reactors

A tubular reactor with measurements at the outlet only is described by the following equations:

$$\frac{\partial}{\partial t} x(t,z) = -\frac{\partial}{\partial z} x(t,z) + f(x(t,z)) \tag{2.4.24}$$

$$y(t) = h(x(t, z = L)) \tag{2.4.25}$$

It should be noted that this model does not include axial diffusion, but only convection.

If we denote with A and C the jacobians of the functions f and h with respect

[1] If $\mathcal{O}$ is full rank, the term $I - \mathcal{O}^+ \mathcal{O}$ simplifies to zero.

to x, we can define their corresponding structure matrices A^* and C^*[2].

The structural observability matrix $\mathcal{S}^*$ is defined as:

$$\mathcal{S}^* = \begin{pmatrix} A^* \\ C^* \end{pmatrix} \tag{2.4.27}$$

A directed graph can be constructed using the matrix $\mathcal{S}^*$, where each nonzero entry $\mathcal{S}_{i,j}$ of the matrix denotes a directed connection (edge) from the vertex j to the vertex i. State vertices are the ones corresponding to the state variables x, output vertices are those corresponding to the output variables y. Ordered sequences of edges without loops are called paths.

The system described by equations 2.4.24 and 2.4.25 is said to be structurally observable if [13]:

- for each state vertex there exists at least one path from this state vertex to at least one of the output vertices;
- the structural rank of the matrix $\mathcal{S}^*$ is equal to the order of the system.

2.4.4 Detectability

A weaker notion than observability is detectability. An unobservable system is said to be detectable if all of the unobservable modes are stable. This implies that even though full state information is not available and some states of the system can only be simulated, the estimation error on the simulated states does not grow unboundedly.

2.4.5 Kalman Filtering

The Kalman filter is the optimal linear estimator for a linear dynamic process with gaussian noise [44]. It works by recursively predicting the current state

[2]The structure matrix M^* of a matrix M is defined as the matrix with elements

$$M^*_{i,j} = \begin{cases} 0 & \text{if } M_{i,j} = 0 \\ * & \text{if } M_{i,j} \neq 0 \end{cases} \tag{2.4.26}$$

The structural rank of M^* is defined as the maximum rank is defined as the maximum rank of all its possible realizations.

estimate given past informations and correcting it as each measurement arrives. Its main strengths are the algorithmic simplicity and the necessity to store very little data at a time.

It is possible to extend its validity to nonlinear systems, although losing optimality, by linearizing the dynamics and the measurement around the current state estimate, hence the name Extended Kalman Filter (EKF). Other nonlinear state estimators exist, such as the unscented Kalman filter or the particle filter, which generally give better performance but demanding significantly more computer power [44, 36].

In this section, the Kalman filter is described for the linear discrete-time case first, then its extension to hybrid continuous-discrete nonlinear systems is discussed.

Description of the system

The dynamics of the system to be estimated are described by the stochastic difference equation:

$$x_{k+1} = F_k x_k + G_k u_k + w_k \tag{2.4.28}$$

where w_k is a vector that represents disturbances in the process dynamics (process noise) and F_k and G_k are the matrices defined in section 2.4.1. w_k is modelled as a discrete, normally distributed, zero mean random variable of covariance Q_k [44]:

$$w_k \sim \mathcal{N}(0, Q_k) \tag{2.4.29}$$

The measurement is described by the equation:

$$y_k = H_k x_k + m_k \tag{2.4.30}$$

where n_k is a vector of measurement noise that is also assumed to be normally distributed, with zero mean and covariance R [44]:

$$m_k \sim \mathcal{N}(0, R_k) \tag{2.4.31}$$

The information carried around by the filter is made of two parts: the state expected value $\hat{x}$, representing the best guess of the filter regarding the plant

Quantity	*A priori*	*A posteriori*
State estimate	$\hat{x}_k^-$	$\hat{x}_k^+$
Error covariance	P_k^-	P_k^+

Table 2.1: Kalman filter estimates

state and the error covariance estimate P, reflecting the amount of uncertainty on individual states [44]. If we denote with $E[\cdot]$ the expected value operator[3]:

$$\hat{x}_k = E[x_k] \tag{2.4.32}$$

$$P_k = E[(\hat{x}_k - x_k)(\hat{x}_k - x_k)^T] \tag{2.4.33}$$

The two estimates can be further specialized to indicate the *a priori* estimate and the *a posteriori* estimate depending on whether the current measurement has been taken into consideration for the estimate. A summary of these quantities is shown in table 2.1.

One possibility to visualize error covariances is to use uncertainty ellipses: since P is a covariance matrix, it has to be positive definite, therefore it is possible to invert it and define the product:

$$(x - \hat{x})^T P^{-1} (x - \hat{x}) = n_\sigma^2 \tag{2.4.34}$$

With n_σ the number of standard deviations for the deviation vector $x - \hat{x}$ with respect to the covariance matrix P. When n_σ is fixed, the product identifies an ellipsoid of constant likelihood in the state space. A higher elongation of the ellipsoid in a certain direction can be seen as a higher uncertainty in such direction.

Prediction-Correction cycle

At each time step, the current *a priori* state estimate is calculated using equation 2.4.28 with the disturbance vector set to zero:

$$\hat{x}_k^- = F_{k-1}\hat{x}_{k-1}^+ + G_{k-1}\hat{u}_{k-1} \tag{2.4.35}$$

[3]The expected value of a random variable is the probability-weighted average of all the possible values of such variable

The state error covariance is propagated as well, to take into account the effect of existing uncertainty and process noise:

$$P_k^- = F_{k-1} P_{k-1}^+ F_{k-1}^T + Q_{k-1} \tag{2.4.36}$$

After a prediction is made, the state estimate is projected on the output space and compared with the measured output. The measurement residual is defined as the difference between the two quantities:

$$r_k = y_k - H_k \hat{x}_k^- \tag{2.4.37}$$

The idea behind recursive estimation is to update the previous state estimate with a corrective term that is proportional to the residual through some gain matrix K_k:

$$\hat{x}_k^+ = \hat{x}_k^- + K_k r_k \tag{2.4.38}$$

The choice of K_k determines the amount of correction and results in the *a posteriori* error covariance P_k [44]:

$$P_k^+ = (I - K_k H_k) P_k^- \tag{2.4.39}$$

$$= (I - K_k H_k) P_k^- (I - K_k H_k)^T + K_k R_k K_k^T \tag{2.4.40}$$

Eq 2.4.40 is called Joseph form of the covariance update and is guaranteed to yield a symmetric matrix (the two forms are equivalent, however the Joseph form is numerically stable [47]).

In the case of the Kalman filter, K_k is chosen such that the *a posteriori* error covariance is minimized:

$$K_k = P_k^- H_k^T \left(H_k P_k^- H_k^T + R_k \right)^{-1} \tag{2.4.41}$$

The expression for the Kalman gain is formally demonstrated by computing the matrix derivative of $\mathrm{tr}(P_k^+)$[4] with respect to K_k and setting it to zero and is described in [44]. A more intuitive explanation is given in [12, 5] and is presented here with the aid of figure 2.4 using the concept of uncertainty ellipses.

[4] $\mathrm{tr}(P)$ denotes the trace of a matrix (the sum of the diagonal elements)

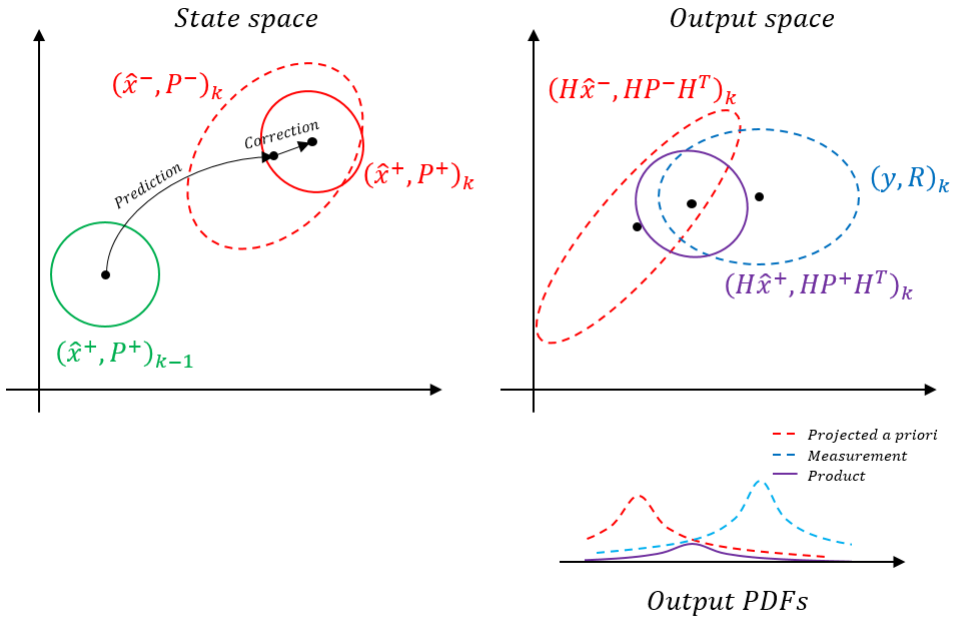

At the beginning of the recursion, the previous a posteriori is known (represented with the green ellipse in the state space). The previous a posteriori is used to predict the current a priori (dashed red ellipse in the state space). This distribution can be projected on the output space and, once a measurement is available, compared with the measurement distribution (represented with the blue dashed ellipse).
The product of the two output distributions is sometimes called overlap, and it is a distribution itself, although not normalized, with its own mean and covariance. The overlap is represented in the output space with the purple ellipse and shown (sliced) in the bottom right plot. The overlap is a measure of the likelihood of a particular output vector given the past knowledge and the current measurement.
The most likely a posteriori estimate is the one that, when projected on the output space, most closely matches the overlap. The Kalman filter gain matrix is calculated accordingly.

Figure 2.4: Representation of the Kalman filter recursion using uncertainty ellipses [12, 5]

Extended hybrid Kalman filter

If the system to be estimated is continuous-time with discrete measurements (hybrid) and nonlinear, it is still possible to use the prediction-correction cycle described in the previous section by linearizing the dynamics and the measurement function around the current state estimate and discretizing [44, 36].

The predicted state estimate $\hat{x}_k^-$ is computed by solving the initial value problem

$$\begin{cases} \dot{x} = f(x, u_k) \\ x(t_{k-1}) = \hat{x}_{k-1}^+ \end{cases} \tag{2.4.42}$$

and setting

$$\hat{x}_k^- = x(t_k) \tag{2.4.43}$$

The measurement residual can be computed as the difference:

$$r_k = y_k - h(\hat{x}_k^-, u_k) \tag{2.4.44}$$

The transition matrix F should be rigorously computed using equation 2.4.10, however this would imply solving the initial value problem 2.4.42 at least $n+1$ times for just a first order approximation[5] with excessive computational costs for large problems.

A much faster approach is to compute A_k, the Jacobian of f, at $\left(\hat{x}_{k-1}^+, u_k\right)$ and then to approximate F_k using equation 2.4.8:

$$F_k \simeq e^{A_k t_s} \tag{2.4.45}$$

The H_k matrix is computed as the Jacobian of h at $\left(\hat{x}_k^-, u_k\right)$.

The evolution of error covariance for linear continuous-time stochastic systems is described by the continuous time Riccati equation [44]:

$$\dot{P} = AP + PA^T + \dot{Q} \tag{2.4.46}$$

where $\dot{Q}$ is the continuous-time analog of the discrete-time process noise co-

[5]The unscented Kalman filter is based on a very similar principle, which however skips the computation of the transition matrix and uses the solutions to better approximate the propagated mean state estimate and covariance.

variance matrix[6].

The *a priori* covariance can be then computed as:

$$P_k^- = P_{k-1}^+ + \int_{t_{k-1}}^{t_k} \dot{P} dt \tag{2.4.47}$$

Numerical methods for the solution of the latter integral will be presented in section 5.2.

Convergence and stability of the Kalman filter

The steady state error covariance of the state estimate for a time invariant system can be computed by setting $P_\infty = P_k^- = P_{k-1}^-$ and performing the relevant substitutions:

$$P_\infty = FP_\infty F^T - FP_\infty H^T (HP_\infty H^T + R)^{-1} HP_\infty F^T + Q \tag{2.4.48}$$

Equation 2.4.48 is commonly referred to as Discrete Algebraic Riccati Equation (DARE).

The steady state gain of the Kalman filter then becomes:

$$K_\infty = P_\infty H^T (HP_\infty H^T + R)^{-1} \tag{2.4.49}$$

For the solution P_∞ to be stable, it is necessary that all of the eigenvalues of :

$$(I - K_\infty H)F \tag{2.4.50}$$

are less than one in magnitude. One necessary condition for this is that the system is detectable [44].

[6]The continuous-time process noise covariance matrix is denoted as $\dot{Q}$ with abuse of notation because it has units $[x]/[t]$, whereas Q has units $[x]$. This notation is not found in literature, where both the continuous-time and the discrete-time process noise covariance matrices are denoted as Q, but was employed here for clearly distinguishing between the two.

2.5 Differential pressure measurement

A differential pressure sensor is a device that measures the difference in pressure between two spaces. Electrical differential pressure sensors (DP cells) allow to transduce the differential pressure into an electric signal.

A DP cell is essentially an assembly of two chambers separated by a deformable membrane that bulges when a differential pressure is applied (shown in figure 2.5a). A resistive element is placed on the membrane [15].

The resistance of an electrical conductor of uniform cross section as a function of its length l, cross-sectional area A and electrical resistivity ρ_{el} can be calculated as:

$$R = \rho_{el}\frac{l}{A} \tag{2.5.1}$$

When the resistive element is deformed it stretches, therefore increasing its resistance. The variation of resistance is captured by a Wheatstone bridge circuit (shown in figure 2.5b) that allows to transduce the resistance variation into a voltage reading V_G [1]:

$$V_G = \left(\frac{R_2}{R_1 + R_2} - \frac{R_x}{R_x + R_3}\right) V_S \tag{2.5.2}$$

The resistive element of the pressure sensor is indicated with R_x. The voltage V_S between A and C, is supplied externally, the output terminals of the DP cell are connected to points B and D and measure the voltage V_G.

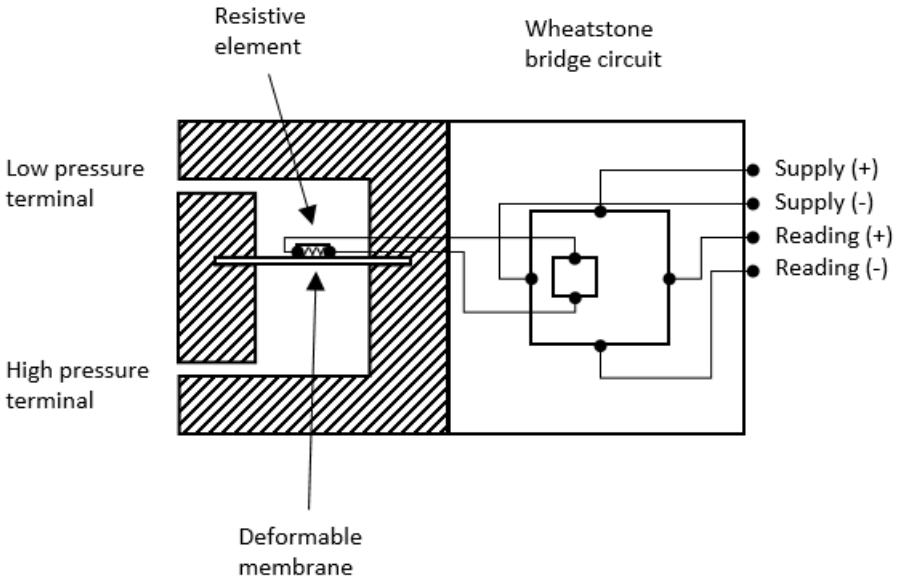

(a) DP cell schematic [45]

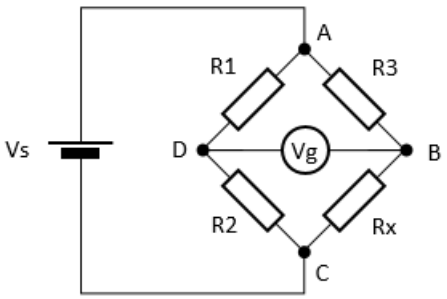

(b) Wheatstone bridge circuit [1]

Figure 2.5: Pressure measurement device

Chapter 3

Plant setup

The plant is built under a fume hood and consists of five sections: the reactant bay with nitrogen purging, the feeding/mixing section with pumps and flowmeters, the CFI reactor (placed inside an oven), the outlet measurement section with the Raman spectrometer, the pressure measurement and a cooling jacket, and finally the product tank. A process flow diagram with the most relevant elements for modelling is presented in appendix B.

3.1 Reactant bay and feeding/mixing sections

Reactants are prepared and placed in bottles. Each bottle is connected to the nitrogen line with a bubbler for purging any dissolved oxygen, as it was found to severely inhibit the reaction [42]. The oven is also purged with nitrogen.

The two initiators (KPS and NaFS) are stored in separate bottles, while the monomers (AA and AMPS) are mixed beforehand.

The reactant bottles are connected to the pumps using dip tubes. Pumping is accomplished using HPLC pumps (double piston type), while flowrate is monitored using Coriolis flowmeters. The mixing of monomers and initiators occurs at T junctions right before entering the oven.

It should be noted that the current configuration of the reactor is not optimal, as it does not allow to dose the monomers independently. The original configuration would involve separate bottles and pumps for each reactant, however due to the malfunctioning of one pump, the setup had to be adapted.

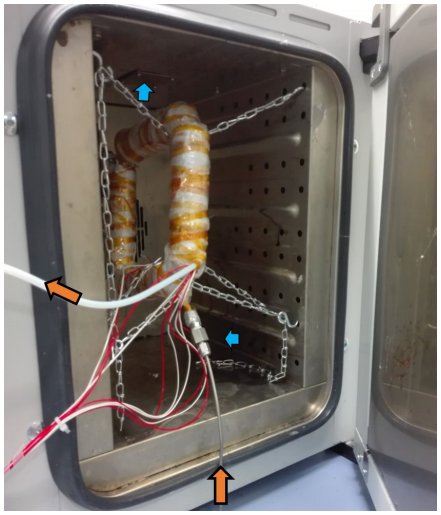

Figure 3.1: Detail of the CFI reactor inside the oven [42]

It is possible to switch the pumps feed to distilled water for startup, shutdown and cleaning phases.

3.2 CFI Reactor

The CFI reactor is built with PTFE tubing coiled around wooden rods. Four temperature sensors (PT100 thermometric resistors) are attached to the reactor pipe using Polyimide tape (thermally stable up to temperatures of ∼300 °C). This configuration only indirectly measures the reactor temperature, however it was chosen as it does not interfere with the Dean vortices and prevents the polymer from sticking and growing near stagnation points [42]. A picture of the CFI reactor mounted inside the oven is shown in figure 3.1, with the orange arrows indicating the flow of the reactants and the blue arrows indicating the flow of the nitrogen.

3.3 Outlet piping

A picture with the various elements of the outlet piping highlighted is displayed in figure 3.2.

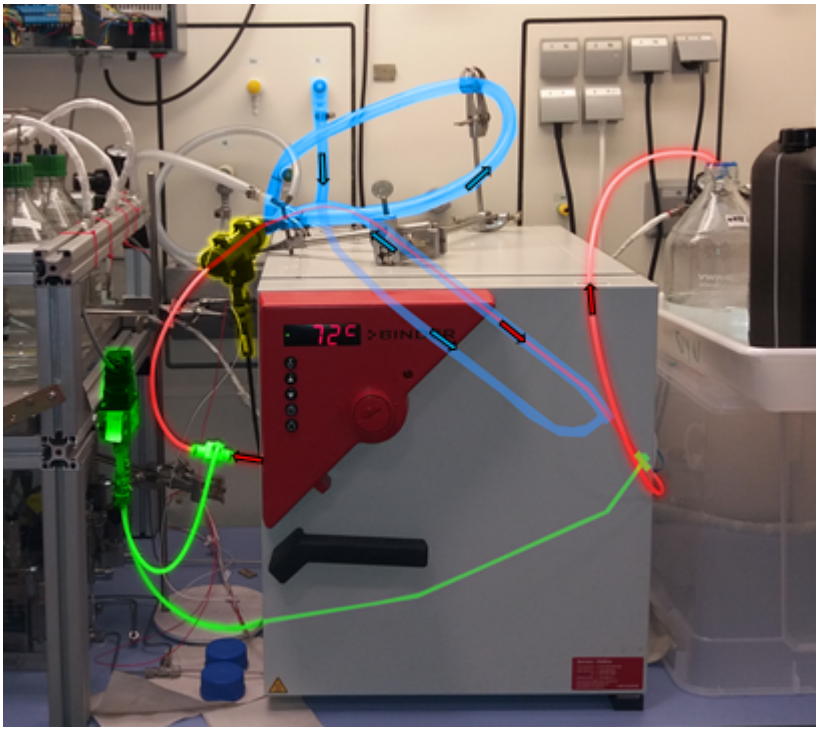

Figure 3.2: Detail of the outlet piping of the plant

When outside the reactor, the polymer-carrying pipe (red) encounters, in this order, the first T-junction for pressure measurement (green), the Raman spectrometer (yellow), the double pipe heat exchanger (blue) and the second T-junction (green) before being collected in the product tanks. The pressure sensor and the heat exchanger were installed in this work.

The two terminals of the pressure sensor are connected with the outlet piping of the reactor using PTFE three way compression fittings, shown in figure 3.3 and placed roughly at the same height in order not to have a biased reading.

When the fitting is assembled and the compression nut fastened, the olive (made in PTFE) wedges between the body of the fitting and tubing, holding the pipe in place by friction. Since the friction factor for PTFE couplings is very low compared with other materials, the maximum internal pressure that the fitting can withstand before bursting is relatively low, thus making it one of the weakest points of the piping.

The pressure-carrying pipes are filled with air to avoid contamination of the product with previous batches of polymer. Using the ideal gas law it is possible

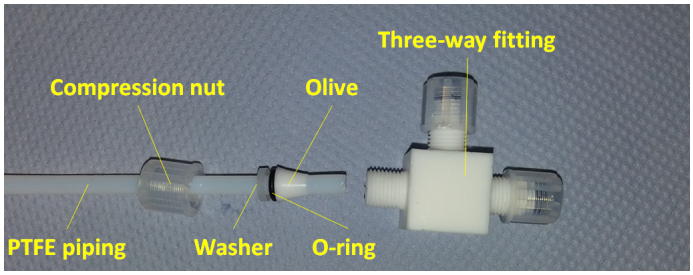

Figure 3.3: Three way compression fitting

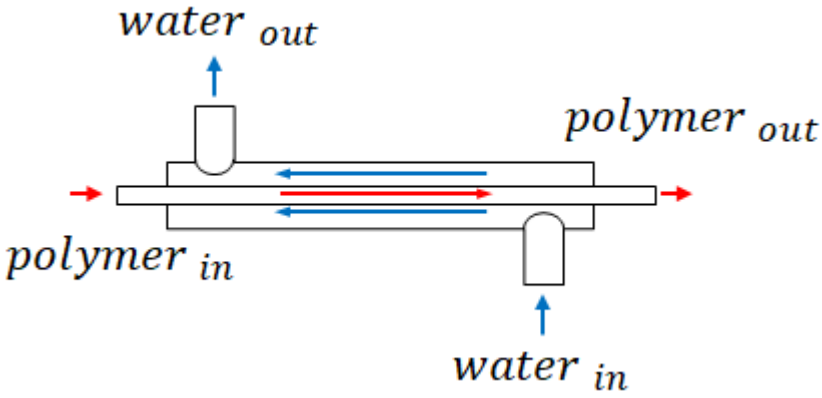

Figure 3.4: Double pipe heat exchanger schematic

to derive a compression factor for the air inside these pipes:

$$\Delta L_{air} = L_{air,0} \cdot \frac{P - P_{atm}}{P} \tag{3.3.1}$$

which, for the high pressure pipe under the assumption of $P = P_{atm} + \Delta P$ can be written as:

$$\Delta L_{air} = L_{air,0} \cdot \frac{\Delta P}{\Delta P + P_{atm}} \tag{3.3.2}$$

With a pressure differential in the order of 0.2 *bar* (taken from experimental data), the compression factor is approximately 0.16 $\frac{cm_{displaced}}{cm_{air,0}}$, meaning that the fluid penetrates 0.16 *cm* inside the pressure pipe for each *cm* initially filled with air.

The cooling jacket (countercurrent double pipe heat exchanger, see figure 3.4) is realized using plastic tubing and custom made glass fittings. Tap water available at 13°C is used for cooling.

The purpose of the cooling jacket is to bring the reactant mixture back to

room temperature in order to slow down the reaction. Once the mixture gets in contact with the outside atmosphere, the dissolving oxygen should poison the residual initiator and inhibit any further reaction.

3.4 Electronics and automation

The sensors and pumps are connected to a computer through an analog-digital converter. The plant is operated using LabView as an interface between the user, the plant and the additional software, such as the Raman spectrum analyzer.

The low-level control of the pumps is automated with a regular PI controller (software-based) that takes a user-defined setpoint.

3.5 Experimental procedure

After installing the new equipment, tests were made to acquire plant data for fitting the pressure drop model.

The experimental procedure is described as follows:

1. Preparations of the reactants;
2. Initial purging of the reactants and water with nitrogen;
3. Initial purging of the reactor with water;
4. Calibration of the Raman spectrometer with monomer feed;
5. Start of the reaction and sampling of the polymer;
6. Final cleaning and shutdown.

The reactants were prepared in three bottles, one with the monomers (AAM and AMPS) and water, the other two with the initiators (KPS and NaFS) and water. This constitutes a deviation from the procedure used in [42], for which the monomers were prepared in different bottles and only mixed at the inlet of the reactor, but was made necessary due to the malfunctioning of one pump. The proportion between the two initiators was left unaltered, although

higher quantities were used (2x, 3x and 4x the concentrations used in [42] were tested).

Another deviation from the previous experimental procedure was to halve the concentration of the monomers, with the aim of mitigating the overpolymerization and clogging of the reactor that was observed in previous runs.

In neither of the experiments it was possible to reach safe steady states, as the temperature inside the reactor and the pump pressure would reach unsafe levels (based on experience) soon after the input flowrate was lowered from $1-1.1$ kg/h to $0.8-0.9$ kg/h.

A number of cloggings were also experienced, with the pressure sensor fittings bursting as soon as the feed pressure reached 10 bar. Additionally, it was found that the fittings constituted preferential spots for polymer clots to grow, thus making the pressure reading less reliable than anticipated.

Due to the number of unsuccesful runs, the laboratory activity was suspended in favor of the development of the EKF tuning procedure. The data that was gathered during the most successful run was tested with the EKF and is presented in section 5.10.

Chapter 4

Plant model

4.1 Reactor

The reactor was modelled (and the model validated) in previous works [42, 9], a brief explanation of the reaction kinetics, mass and heat transport and discretization is presented in the following sections for clarity.

4.1.1 Reaction kinetics

The reaction rates are written for the elementary reactions described in section 2.1.1. The order of reaction is assumed to be equal to the reaction molecularity (law of mass action), and the temperature dependence is assumed to follow Arrhenius law:

$$k_j = k_{j,\infty} \cdot e^{-\frac{E_a}{RT}} \tag{4.1.1}$$

Once the kinetic model is developed in terms of the individual polymer chains, the method of moments is used to rewrite the expressions for the reaction rates in terms of the polymer moments P_{10}, P_{11}, P_{12}, P_{20}, P_{21}, P_{22}, D_0, D_1, D_2 [32] by factoring them out in 2.1.24. The expressions for the reaction rates are summarized here for the various species in appendix A.1.

4.1.2 Mass transport

The conservation equations (expressed in terms of concentrations) are written in one spatial dimension using a dispersion model:

$$\frac{\partial c_j}{\partial t} = -v \cdot \frac{\partial c_j}{\partial z} + \frac{\partial}{\partial z} \cdot \left(D_{ax} \cdot \frac{\partial c_j}{\partial z} \right) + r_j \tag{4.1.2}$$

Here D_{ax} is the axial dispersion coefficient that incorporates all the mass transfer effects that result from the enhanced radial mixing. The dispersion coefficient is correlated to the flow conditions, the geometry of the reactor and the properties of the fluid through three dimensionless numbers: Re (Reynolds number), Sc (Schmidt number) and Bo (Bodenstein number). The correlations are presented more in depth in section A.2, for the purpose of state estimation it suffices to say that:

$$D_{ax} = D_{ax}\left(F, \omega\right) \tag{4.1.3}$$

with F the volume flowrate of the system and ω the weight fraction of the polymer.

Equation 4.1.2 can be specialized for each concentration state of the model by appropriately writing the generative term r (the dispersion coefficient is assumed to be the same for every component of the mixture). The expression is valid also for the transport of moments, as it was anticipated in section 2.1.2.

The problem is completed with the boundary conditions.

A Danckwerts boundary condition was chosen for the inlet of the reactor:

$$v c_{j,\text{feed}} = v c_j(z = 0, t) - D_{ax} \left. \frac{\partial c_j}{\partial z} \right|_{z=0} \tag{4.1.4}$$

meaning that the total molar flux (given by convection and back diffusion) at the inlet of the reactor is equal to the molar flux at the feeding section.

The outlet of the reactor is assumed to be described by a zero gradient (Neumann) boundary condition:

$$0 = \left. \frac{\partial c_j}{\partial z} \right|_{z=L} \tag{4.1.5}$$

4.1.3 Heat transport

The heat transfer is modelled by two energy balances equations, one for the fluid and one for the pipe (which resistance cannot be neglected). Two temperatures are kept track of: the reactor fluid temperature (T_r) and the tube temperature (T_t). Heat is assumed to only propagate in the axial direction by convection.

$$\frac{\partial T_r}{\partial t} = -v \cdot \frac{\partial T_r}{\partial z} + \frac{\Delta H_r}{\rho \cdot C_P} \cdot r + \frac{UA_2}{C_P \cdot \rho \cdot A_{q,f} \cdot L} (T_t - T_r) \tag{4.1.6}$$

$$\frac{\partial T_t}{\partial t} = \frac{UA_2}{C_{P,t} \cdot \rho_t \cdot A_{q,t} \cdot L} (T_r - T_t) + \frac{UA_1}{C_{P,t} \cdot \rho_t \cdot A_{q,t} \cdot L} (T_o - T_t) \tag{4.1.7}$$

with $A_{q,f}$ the cross-sectional area of the fluid and $A_{q,t}$ the cross-sectional area of the pipe.

The properties of the tube are indicated with the subscript t. The reaction enthalpies ΔH_r are fitted from experimental data. The fluid side overall heat transport coefficient UA_2 can be determined from correlations in terms of Re, Pr (Prandtl number) and Nu (Nusselt number) and is shown in detail in section A.3. The oven overall heat transport coefficient UA_1 is fitted and the temperature of the oven is indicated with T_o and is known.

The inlet temperature is specified as a boundary condition.

4.1.4 Discretization

The system is described by 18 state variables that are both functions of axial position and time. As it was anticipated in section 2.4.1, however, the spatial dependence is discretized in order to make the problem tractable numerically. The length of the reactor is approximated with 15 internal grid points (the inlet and outlet boundaries count as two additional grid points) and the spatial derivatives approximated with an explicit finited differences method. The number of grid points is the result of a tradeoff between accuracy and performance of the model [42].

The full set of state variables and the vectorization of the state matrix are shown in section A.4.

4.2 Outlet piping

The pressure drop model for the outlet piping and the correlation between viscosity and the state variables were developed in this work.

4.2.1 Pressure drop model

The pressure drop model is derived by specializing the general momentum balance equation [8]:

$$\rho \cdot \left(\frac{\partial v}{\partial t} + v \bullet \nabla u \right) = \nabla \bullet \tau - \nabla P + \rho g \tag{4.2.1}$$

A cylindrical coordinate system is chosen to describe the problem. The flow is assumed to be unidirectional in the axial direction z and to evolve along the radial direction r. The convection term in the momentum equation is neglected and the problem is assumed to be stationary.

This assumption should be verified by demonstrating that the characteristic timescale of the process t_p is greater than the fluid-dynamics timescale, which can be determined by comparing the characteristic values of the time derivative with the pressure drop term:

$$\rho \cdot \frac{F_c/R^2}{t_f} \sim \frac{\Delta P_c}{L} \tag{4.2.2}$$

$$t_f \sim \frac{\rho \cdot F_c}{\Delta p_c} \cdot \frac{L}{R^2} \tag{4.2.3}$$

The fluid dynamics time scale is found to be in the order of $9.3 \cdot 10^{-4}$ s[1], therefore the stationarity hypothesis is deemed reasonable.

The process timescale should also be greater than the polymer relaxation time, which is expected to be in the order of 1 s, for the elastic effects to be negligible (see section 2.1.3).

The problem is completed by the boundary layer conditions at $r = 0$ (simmetry condition) and $r = R$ (no-slip condition). The pressure at $z = 0$ is left

[1] Using a mass flowrate of 0.4 kg/h, a pressure drop of 0.2 bar over a length of 1.5 m and a pipe radius of 3 mm.

unspecified since we're only interested in the pressure drop over a section of the pipe.

The full set of equations can be written in dimensional form:

$$\begin{cases} -\dfrac{\partial p}{\partial z} = \dfrac{1}{r} \cdot \dfrac{\partial}{\partial r}\left(r \cdot \tau\right) \\ \tau = \tau(\dot{\gamma}) \\ \dot{\gamma} = \dfrac{\partial v}{\partial r} \\ \tau|_{r=0} = 0 \\ v|_{r=R} = 0 \\ P|_{z=0} - P|_{z=L} = \Delta P \end{cases} \tag{4.2.4}$$

An additional equation is provided to link the local velocity to the volume flowrate in a section of pipe:

$$F = \int_0^R v(r) \cdot 2\pi \cdot r dr \tag{4.2.5}$$

Reference flow model

In order to faithfully capture the physical behaviour of the polymer mixture flow inside the apparatus, a truncated power law model (Spriggs model [7]) is chosen to describe the stress-shear rate function. This model is based on three parameters: zero shear rate viscosity (η_0), transition shear rate ($\dot{\gamma}_0$) and power law exponent (n). The transition zone between Newtonian and power law behaviour that is typically observed is regarded as infinitely small, thus ignoring the effect of polymer distribution. The error introduced from this approximation should be reasonably small for engineering purposes.

$$\tau(\dot{\gamma}) = \begin{cases} -\eta_0 \cdot \dot{\gamma} & \dot{\gamma} < \dot{\gamma}_0 \\ -\eta_0 \cdot \left|\frac{\dot{\gamma}}{\dot{\gamma}_0}\right|^{n-1} \cdot \dot{\gamma} & \dot{\gamma} \geq \dot{\gamma}_0 \end{cases} \tag{4.2.6}$$

This model has several perks: it's simple enough to allow for analytical integration but at the same time it contains the most significant parameters (which can eventually be connected to the polymer solution's properties).

It's possible to express the boundary value problem 4.2.4 in terms of dimensionless variables, i.e: $y^* = y/y_0$, with

$$r_0 = R \tag{4.2.7}$$

$$dz_0 = L \tag{4.2.8}$$

$$\tau_0 = \eta_0 \cdot \dot{\gamma}_0 \tag{4.2.9}$$

$$v_0 = R \cdot \dot{\gamma}_0 \tag{4.2.10}$$

$$dP_0 = \frac{L}{R} \cdot \eta_0 \cdot \dot{\gamma}_0 \tag{4.2.11}$$

$$F_0 = 2\pi \cdot R^3 \cdot \dot{\gamma}_0 \tag{4.2.12}$$

The set of equations then becomes:

$$\begin{cases} -\dfrac{\partial P^*}{\partial z^*} = \dfrac{1}{r^*} \cdot \dfrac{\partial}{\partial r^*} \cdot (r^* \cdot \tau^*) \\ \tau^* = \tau^*(\dot{\gamma}^*) \\ \dot{\gamma}^* = \dfrac{\partial v^*}{\partial r^*} \\ \tau^*|_{r^*=0} = 0 \\ v^*|_{r^*=1} = 0 \end{cases} \tag{4.2.13}$$

with:

$$F^* = \int_0^1 v^*(r^*) \cdot r^* dr^* \tag{4.2.14}$$

Since the derivatives in the partial differential equation are independent of each other, the problem can be solved by introducing a constant k:

$$-\frac{\partial P^*}{\partial z^*} = k \tag{4.2.15}$$

$$\frac{1}{r^*} \cdot \frac{\partial}{\partial r^*}(r^* \cdot \tau^*) = k \tag{4.2.16}$$

From the definition, k is a positive number representing the dimensionless pressure drop over a unit characteristic length.

The second differential equation can be solved by separation of variables, leading to:

$$\tau^* = \frac{k}{2} \cdot r^* \tag{4.2.17}$$

Two regimes of viscosity are in general possible: in the innermost cylindrical region, where the shear rate does not exceed the transition value, the fluid behaves as Newtonian. Outside of this region the shear rate exceeds the transition value and the fluid exhibits the power-law behaviour. A transition radius r_t^* can be found by setting the dimensionless stress to 1:

$$r_t^* = \frac{2}{k} \tag{4.2.18}$$

If the critical radius exceeds 1, the flow is entirely Newtonian. In general, however, the transition shear rate is so small that the transition radius is much smaller than the pipe radius.

The relevant stress expression is substituted in the equation and the integration completed to get the velocity profile $v^*(r^*)$:

$$v^*(r^*) = \begin{cases} \frac{1}{k} + \frac{\left(\frac{k}{2}\right)^{\frac{1}{n}}}{\frac{1}{n}+1} \cdot \left(1 - \left(\frac{2}{k}\right)^{\frac{1}{n}+1}\right) - \frac{k}{4} r^{*2} & r^* < r_t^* \\ \frac{\left(\frac{k}{2}\right)^{\frac{1}{n}}}{\frac{1}{n}+1} \cdot \left(1 - r^{*\frac{1}{n}+1}\right) & r^* \geq r_t^* \end{cases} \tag{4.2.19}$$

An expression for the dimensionless flowrate is then obtained as a function of k and n by integrating eq. 4.2.19:

$$F^* = \begin{cases} \frac{2^{-1-\frac{1}{n}}}{k^3 \cdot (n-1) \cdot (3n-1)} \left(n \cdot (n+1) \cdot k^{\frac{1}{n}+2} + 2^{\frac{1}{n}+1} n^2 + 2^{\frac{1}{n}+1} \cdot (1 - 9n^2)\right) & \text{for } k > 2 \\ \frac{k}{16} & \text{for } k \leq 2 \end{cases} \tag{4.2.20}$$

The relationship between flowrate and pressure drop is monotonic for positive values of k, but cannot be inverted analitically. This is not a problem in practice, as this model only serves as a benchmark for the operational model.

Power law flow model

A simplified representation of the fluid can be done by disregarding the Newtonian plateau at low shear rates. This approximation is usually acceptable for practical purposes. The stress term is modelled with a power law function,

with the parameters K (proportionality constant) and n (power law exponent).

$$\tau(\dot{\gamma})_{pl} = -K \cdot |\dot{\gamma}|^{n-1} \cdot \dot{\gamma} \tag{4.2.21}$$

The parameter K can be traced back to the material functions η_0 and $\dot{\gamma}_0$ of the reference model via the relation:

$$K = \frac{\eta_0}{\dot{\gamma}_0^{n-1}} \tag{4.2.22}$$

Conversely to the reference flow one, this model will be used to interpret the differential pressure measurement to evaluate K. The power law slope is assumed to be known beforehand.

The boundary value problem in eq. 4.2.4 is specialized with the new expression for τ and solved for ΔP:

$$\Delta P = 2 \cdot \left(\frac{1+3n}{\pi \cdot n}\right)^n \cdot K \cdot L \frac{F^n}{R^{3n+1}} \tag{4.2.23}$$

The previous expression can be inverted in order to make K explicit:

$$K = \frac{1}{2}\left(\frac{\pi \cdot n}{1+3n}\right)^n \frac{\Delta P}{L} \cdot \frac{R^{3n+1}}{F^n} \tag{4.2.24}$$

We now wish to evaluate the error between K and the ratio:

$$e = \frac{K - \frac{\eta_0}{\dot{\gamma}_0^{n-1}}}{\frac{\eta_0}{\dot{\gamma}_0^{n-1}}} \tag{4.2.25}$$

To do this we substitute $\Delta P = k \cdot \dfrac{L}{R} \cdot \eta_0 \cdot \dot{\gamma}_0$ (from eq.4.2.11) and $F = 2\pi \cdot R^3 \cdot \dot{\gamma}_0 \cdot F^*(k)$ (from eq. 4.2.12) in eq. 4.2.24, under the assumption that the n used in the power law model is the same as the one used in the Spriggs model.

After some simplifications we obtain:

$$e = 2^{-1-n}\left(\frac{n}{1+3\cdot n}\right)^n \frac{k}{F^*(k,n)^n} - 1 \tag{4.2.26}$$

This error is generally small (under 1%) except for very low values of F^* or n, in which cases the Newtonian regime is found in an extensive region of

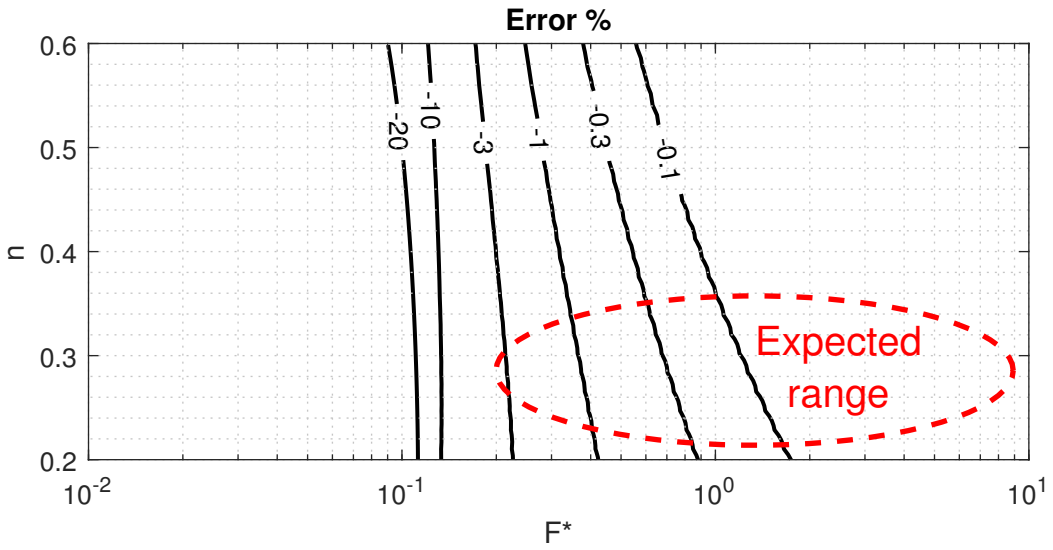

Figure 4.1: Error map for the power law approximation

the domain and K is underestimated. A map of the approximation error is provided in figure 4.1 together with the expected (and conservative) region of operation[2].

4.2.2 Connection between viscosity and the state variables

In order to correlate viscosity to the state variables of the polymer solution we take advantage of the fact that K can be used to approximate the ratio $\frac{\eta_0}{\dot{\gamma}_0^{n-1}}$. The fitness of this approximation is good as long as the value of n used for the measurement is reasonably close to the true value and the region of Newtonian flow is negligible in size with respect to the total flow surface.

We know from 2.1.28, 2.1.30 and 2.1.31 that η_0 and $\dot{\gamma}_0$ are powers of the first and second moments and viscosity depends exponentially on temperature.

A generalized expression for K is proposed as follows:m

$$K(Q_1, Q_2, T) = e^a \cdot Q_1^b \cdot Q_2^c \cdot e^{\frac{d}{T}} \tag{4.2.27}$$

This function can be linearized by taking the natural logarithm. This allows

[2]A value of $\dot{\gamma}_0 \in [0.1, 1]\ s^{-1}$ (from [16]) was used to compute F_0.

to determine parameters via linear least squares given experimental data.

$$\ln(K) = a + b \cdot \ln(Q_1) + c \cdot \ln(Q_2) + d \cdot \frac{1}{T} \tag{4.2.28}$$

4.2.3 Mass and heat transport

The models for viscosity presented so far are valid under the assumptions of constant composition and temperature along the pipe. Clearly this is not the case for the outlet pipe, which is too long (in relation to the flowrate) for the assumption of constant composition to be valid during transitories. Moreover, the cooling of the reaction mixture determines a drastic change in the viscosity of the fluid that should be accounted for.

Luckily, the balance equations governing the problem are the same as the ones presented in sections A.3 and A.2, and it's only necessary to adapt the correlations to the new geometry (which can be approximated as a straight pipe).

The dispersion coefficient can be computed for laminar flow in straight pipes with the Taylor-Aris correlation [38]:

$$Bo = \left(\frac{1}{Re \cdot Sc} + \frac{Re \cdot Sc}{192} \right)^{-1} \cdot \frac{L}{d_{in}} \tag{4.2.29}$$

The fluid-side heat transfer coefficient can be calculated using the forced convection correlation from [29] for power-law fluids in horizontal straight pipes:

$$Nu = 1.41 \cdot \left(\frac{3n+1}{4n} \right)^{1/3} \cdot Gz \cdot \left(\frac{K}{K_p} \right)^{\frac{0.1}{n^{0.7}}} \tag{4.2.30}$$

where Gz (Graetz number) is a dimensionless number, and K_p is the non-newtonian viscosity coefficient computed at the pipe temperature:

$$Gz = \frac{F_w C_P}{\lambda L} \tag{4.2.31}$$

The outer heat transfer coefficient U is written for the jacketed section as:

$$U = \frac{Nu_j \cdot \lambda_w}{D_H} \tag{4.2.32}$$

with D_H the hydraulic diameter of the jacket.

The Nusselt number for the jacket is computed as[15]:

$$Nu_j = 0.027 \cdot Re_j^{0.8} Pr_j^{1/3} \tag{4.2.33}$$

with Re_j the Reynolds number for water in the outer pipe (using the hydraulic diameter as a characteristic length) and Pr_j the Prandtl number of water.

4.3 Measured variables

The measured set consists of four pipe temperatures, two monomer concentrations, one pressure measurement and 15 fictitious first moment measurements:

$$y_m = \begin{pmatrix} T_{1m} & T_{2m} & T_{3m} & T_{4m} & c_{\mathrm{M}_1 m} & c_{\mathrm{M}_2 m} & \Delta p_m & Q_{1,1m} & \dots & Q_{1,15m} \end{pmatrix}^T$$

4.3.1 Reactor pipe temperatures

The measurement of the $i-$th thermometer resistance is modelled through an energy balance:

$$m_s \cdot C_{P,s} \cdot \frac{\partial T_{im}}{\partial t} = \frac{UA_{oven}}{L} \cdot (T_o - T_{im}) + \frac{UA_{tube}}{L} \cdot (T_t - T_{im}) \tag{4.3.1}$$

The accumulation term can be neglected due to the small mass of the sensor, therefore the temperature of the sensor can be rewritten as:

$$T_{im} = \nu_i \cdot (T_o - T_t) + T_t \tag{4.3.2}$$

Where $\nu_i \in [0; 1]$ is a parameter that contains the heat transfer coefficients of the system.

4.3.2 Monomer concentrations

The outlet monomer concentration is measured by the means of Raman spectroscopy. The spectrum of the Raman spectrometer is sampled and digitally processed with an algorithm developed in [9] to obtain an area intensity vector

I. The purpose of this part of the signal processing is to remove the influence of the materials of the Raman spectrometer and water from the measured spectrum and to have a more robust reading against disturbances.

The concentration of the monomers can be then computed as:

$$\begin{pmatrix} c_{\mathrm{M}_1} \\ c_{\mathrm{M}_2} \end{pmatrix}_m = \Gamma I \tag{4.3.3}$$

where Γ is a matrix obtained by calibration.

The measurement function employed in the Kalman filter is

$$\begin{pmatrix} c_{\mathrm{M}_1} \\ c_{\mathrm{M}_2} \end{pmatrix}_m = \begin{pmatrix} c_{\mathrm{M}_1} \\ c_{\mathrm{M}_2} \end{pmatrix}_{out} \tag{4.3.4}$$

4.3.3 Pressure drop

The pressure drop in the outlet piping of the plant is modelled using the model 4.2.23:

$$\Delta p_m = 2 \cdot \left(\frac{1+3n}{\pi \cdot n} \right)^n \cdot L \cdot \frac{F^n}{R^{3n+1}} \cdot \frac{1}{N} \cdot \sum_{j=1}^{N} K_j \tag{4.3.5}$$

with

$$K_j = e^a \cdot (P_{11,j} + P_{21,j} + D_{1,j})^b \cdot (P_{12,j} + P_{22,j} + D_{2,j})^c \cdot e^{\frac{d}{T_j}} \tag{4.3.6}$$

where the subscript j denotes the corresponding variable taken at the $j-$th discretization point of the outlet piping.

4.3.4 Overall first moment

The first moment of a polymeric mixture is defined as the sum of the molar concentration of polymer chains of length k times the chain length, extended to all possible chain lengths

$$Q_1 = \sum_{k=0}^{\infty} k c_k \tag{4.3.7}$$

and it can be seen as the number of monomeric units consumed per unit volume to form the existing polymer chains.

If we consider the integral molar balance of the monomers between the inlet of the reactor and the section z:

$$\frac{dn_{\mathrm{M}[0,z]}}{dt} = \dot{n}_{\mathrm{M},0} - \dot{n}_{\mathrm{M},z} - \dot{n}_{\mathrm{M},r[0,z]} \tag{4.3.8}$$

where $\dot{n}_{\mathrm{M},r[0,z]}$ is the integral rate of reaction of the monomer between the inlet and the section z.

If we assume constant density we can rewrite the previous equation in terms of molar concentrations

$$\frac{V_{[0,z]}}{F}\frac{d\bar{c}_{\mathrm{M}[0,z]}}{dt} = c_{\mathrm{M},0} - c_{\mathrm{M},z} - \frac{n_{\mathrm{M},r[0,z]}}{V_{[0,z]}} = c_{\mathrm{M},0} - c_{\mathrm{M},z} - Q_{1,z} \tag{4.3.9}$$

and if we disregard the accumulation term and we rearrange we obtain:

$$c_{\mathrm{M},z} + Q_{1,z} = c_{\mathrm{M},0} \tag{4.3.10}$$

Since the concentration of the monomers at the inlet section is known, we can treat this equation as a fictitious measurement in any point of the reactor:

$$Q_{1m} = c_{\mathrm{M}_1} + c_{\mathrm{M}_2} + P_{11} + P_{21} + D_1 = \left(c_{\mathrm{M}_1} + c_{\mathrm{M}_2}\right)_0 \tag{4.3.11}$$

Chapter 5

State estimation

5.1 Observability study

Before going deeper into the practical aspects of the state estimator, an observability study is presented.

The method described in section 2.4.3 is used to represent the connection between state variables and measurements. The graph in figure 5.1 displays the shortest path trees from the individual states to the measured outputs. The contribution of the diffusive term is disregarded in this analysis to conform with the method presented by [13] and so are the connections with the overall first moment fictitious measurement.

From the graph it is already possible to see that some state variables (co_{M_1}, co_{M_1}, D_0) don't belong to paths that can influence the measured outputs, therefore they are completely invisible to the observer (making the system globally unobservable). The monomer consumption tracking states appear to be disconnected as they only appear in the diffusive term of the mass transfer equation 4.1.2, which is neglected in this analysis.

All the modes of the system are stable at any operating point of interest (the eigenvalues of F for a typical steady state are shown in figure 5.2), therefore the system is detectable according to the definition in section 2.4.4.

Due to the size of the discretized model (270 state variables) and its strong nonlinearity, it is impossible to perform a rigorous nonlinear observability analysis. It is possible to linearize the system around selected operating points and assess local observability using the methods presented in section 2.4.3.

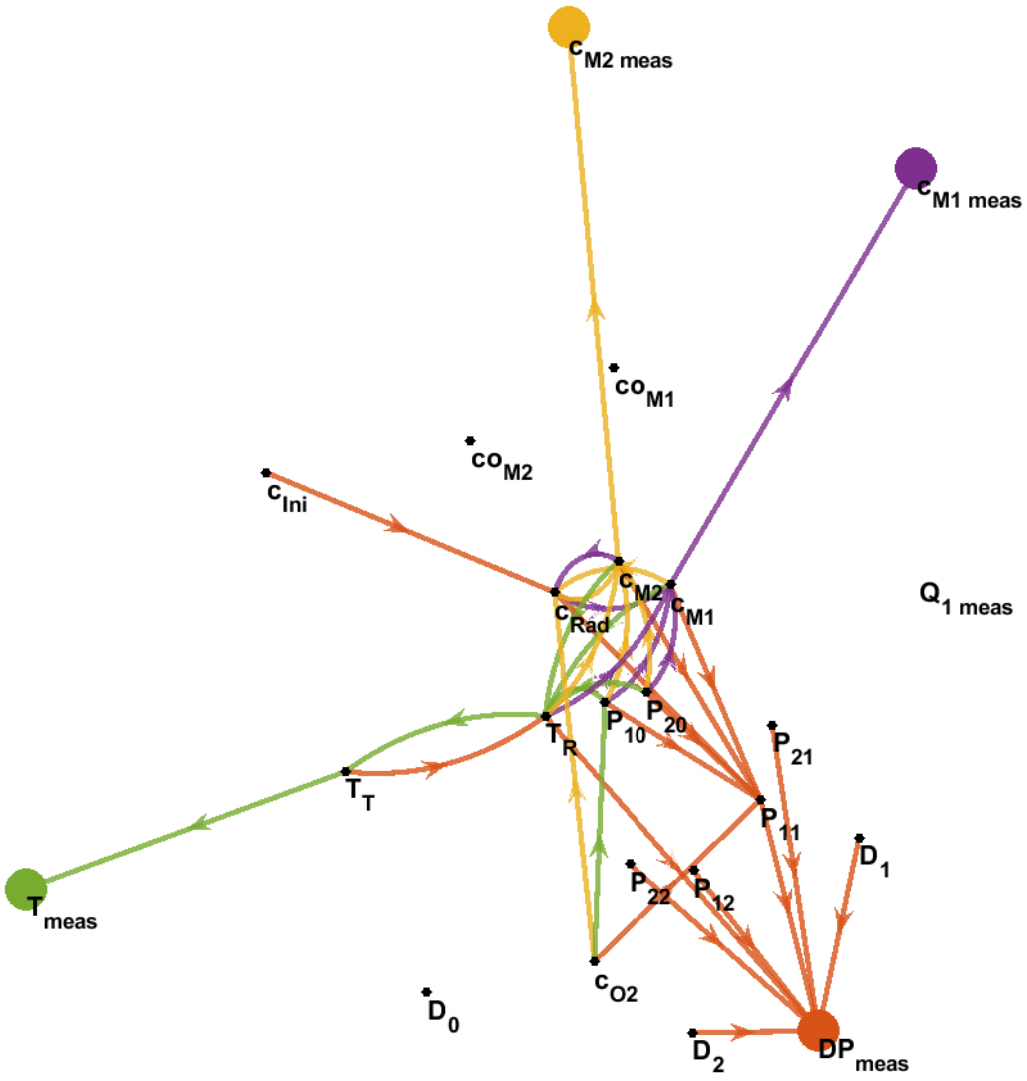

Figure 5.1: State - measurement connection graph [13]

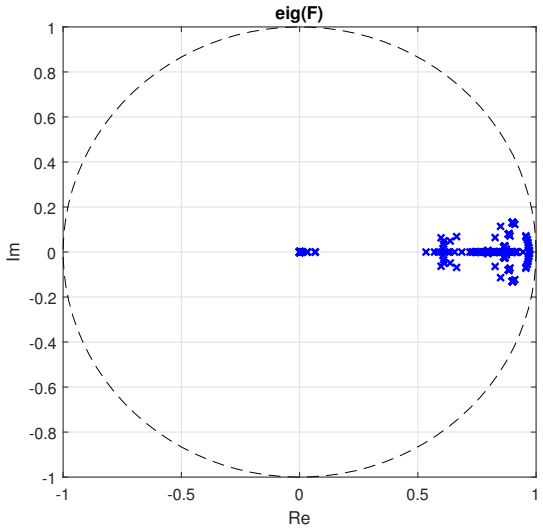

Figure 5.2: Eigenvalues of the state transition matrix F

If linear observability criteria are used, the outcome could be severely affected by the conditioning of the matrices: numerically constructing the Kalman observability matrix 2.4.17 for a system of such size is likely to result in numerical overflow. It was found in simulations that the continuous-time observability criteria would be more susceptible to failures than the discrete-time tests. This is demonstrated in figure 5.3, where the matrix condition number for the matrix powers A^k and F^k is plotted for increasing k. Clearly, the continuous-time observability criterion would be much more numerically unstable than the discrete-time one as it involves the computation of the matrix power A^k.

Even if a more robust method such as the Hautus criterion is used, the matrix rank check could still give incorrect results[1].

The discrete-time unobservability index method was tested and the results are presented here in figures 5.4a, 5.4b, 5.4c and 5.4d, where observable states are marked with dots and the degree of unobservability is represented with different shades of colour. It was found that at different steady states the unobservability maps do not change significantly, as it is shown in figure 5.4a. During flowrate changes, however, the system becomes less observable, (figure 5.4b).

[1]Most numerical packages check the rank of a matrix by performing its singular value decomposition and counting the number of singular values greater than some tolerance. If the matrix is full rank but poorly conditioned (for example, if it's very big in size), some

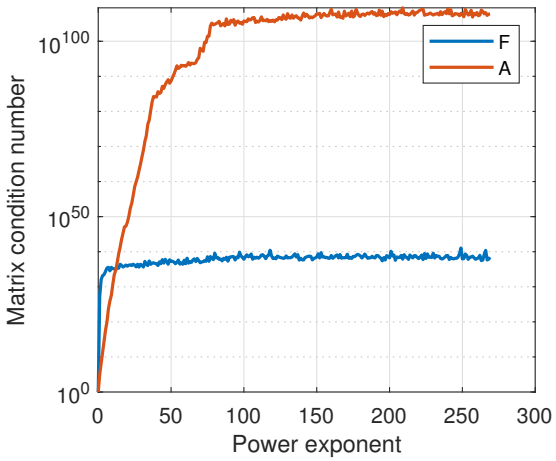

Figure 5.3: Matrix condition number for the matrix powers A^k and F^k

Compared to the previous configuration, the addition of the pressure drop measurement at the outlet improves the observability of the system only partially (figure 5.4c). The states that are most clearly affected by the pressure drop information are the first moments of the live and dead polymer chains, and to some extent the second moments of the live polymer chains.

Partial observability, recalling the definitions of section 2.4.3, relates to the fact that the initial value of partially observable states, given a vector of measurements, can be expressed as the combination of one definite solution and one free solution using equation 2.4.23, with the unobservability index reflecting the weight of the free solution.

In the case of the CFI reactor, the pressure drop information only partially improves the observability of the newly measured states, because the reading depends on a combination of states with similar dynamics. The first moment constraint appears to have a worsening effect on the observability of some previously observable states, but this was found to be caused by the automatic tolerance set by Matlab in computing the pseudoinverse. As it will be shown in 5.9.1, the first moment constraint has a beneficial effect in state estimation in that it reduces the violation of the monomer mass balance.

It was found that, in addition to D_0, other state variables are practically unobservable. It is the case of the $c_{\mathrm{R}\bullet}$ and c_{O_2} states, for example, which are characterized by fast dynamics and comparatively small numeric values. De-

singular values could be treated as zeros even though in reality they are not [35].

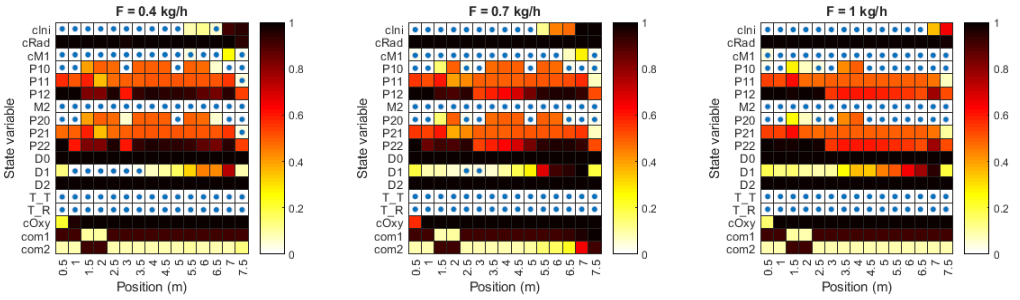

(a) Steady state unobservability index at different flowrates

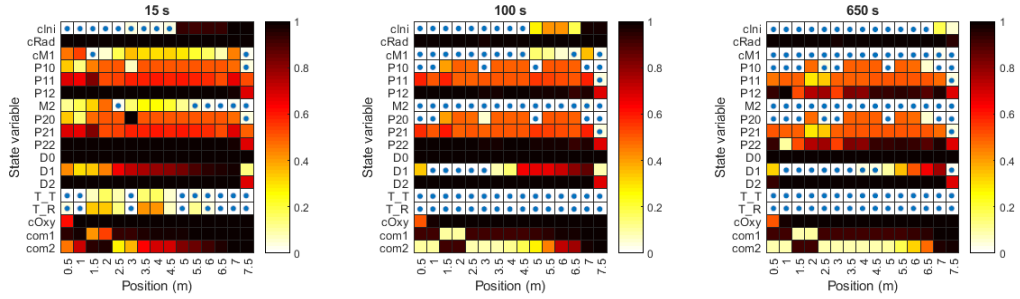

(b) Unsteady state unobservability index during flowrate step

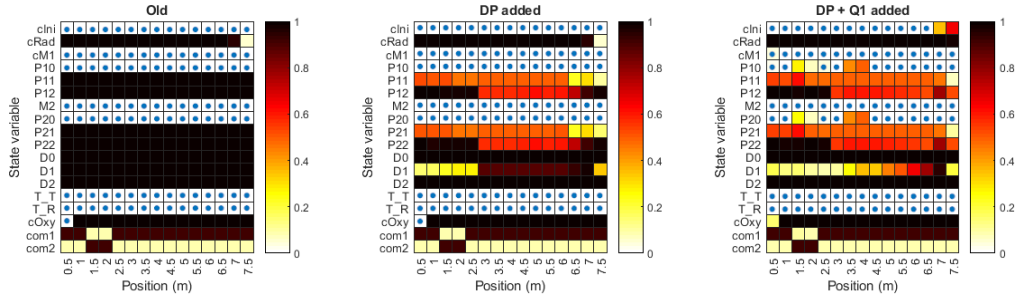

(c) Steady state unobservability index for different measured sets

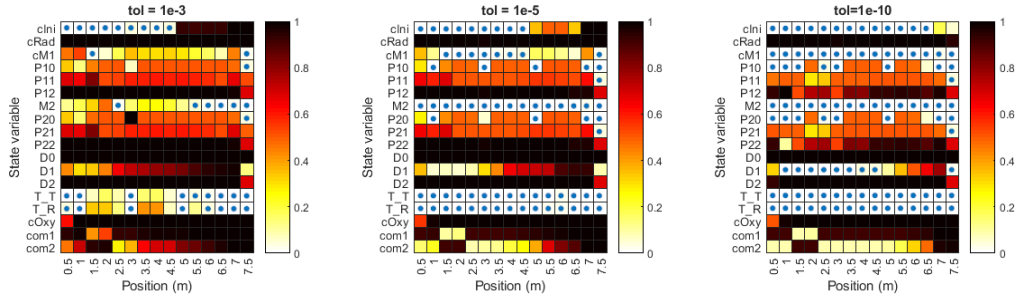

(d) Steady state unobservability index for different pseudoinverse tolerances

Figure 5.4: Method of the unobservability indices [21]

spite being measured, D_2 appears to be mostly, if not completely, unobservable, possibly because of its small magnitude compared with P_{12} and P_{22} or because of the way it interacts with the pressure drop in relation to the other measured states. This is not clear from the graph analysis of figure 5.1, however by inspecting the reaction kinetics of A.1 it is possible to see that, while the live polimer chain moments enter in both the live polymer kinetics and the dead polymer kinetics, the dead polymer chain moments only act as sinks for the other state variables before being measured. This type of interplay is thought to be at the roots of the observability behaviour.

One remark should be made regarding the practical use of these unobservability indices: when computing the Moore-Penrose inverse of $\mathcal{O} \in \mathbb{R}^{m \cdot n \times n}$ (see section 2.4.3) with numerical packages, the truncation tolerance is chosen by default as

$$\text{tol} = m \cdot n \cdot \epsilon(||\mathcal{O}||_2) \tag{5.1.1}$$

where $\epsilon(x)$ is the positive distance from $|x|$ to the next larger floating point number. If a different tolerance is chosen, the results can change (a larger tolerance will result in more states appearing as unobservable and viceversa). This is demonstrated in figure 5.4d, where the unobservability test was repeated different tolerances, showing a sheer decrease in the number of the completely observable states as the tolerance is increased.

The authors of the unobservability indices method suggest to choose the pseudoinverse tolerance to skim off those states that are most affected by noise [21], though not providing a clear criterion for this choice. One possibility would be to rescale the H matrix with respect to the noise standard deviation before computing $\mathcal{O}$, such that the singular values of the observability matrix reflect the signal to noise ratio of the individual states on the output measurement.

5.2 Discretization of the prediction step

The integration of the continuous time Riccati equation by numerical methods is particularly hard since the problem grows in size with the square of the number of states and is severely complicated by ill-conditioned model jacobians. Under the assumptions of constant A and $\dot{Q}$ during the sampling interval of size t_s, however, exact solutions exist for the Riccati equation 2.4.46 in the

Algorithm 5.1 Time discretization of the process noise covariance matrix [48]

1. Compute $F = e^{At_s}$
2. Compute $V = \dot{Q} - F\dot{Q}F^T$
3. Compute Q as the solution of the continuous-time Lyapunov equation:

$$AQ + QA^T = -V \tag{5.2.5}$$

form:

$$P_{k+1}^- = F_k P_k^+ F_k^T + Q_k \tag{5.2.1}$$

where F is the matrix exponential

$$F_k = e^{A_k t_s} \tag{5.2.2}$$

and Q_k is the solution of the integral

$$Q_k = \int_0^{t_s} e^{A_k t} \dot{Q}_k e^{A_k^T t} dt \tag{5.2.3}$$

Since A and $\dot{Q}$ could be, in principle, functions of time, it's possible to increase the accuracy of the solution by replacing A_k with $\frac{1}{2}(A_k + A_{k+1})$ and $\dot{Q}$ with $\frac{1}{2}(\dot{Q}_k + \dot{Q}_{k+1})$ in the previous equations.
A crude approximation of the integral 5.2.3 in is the following:

$$Q_k = \dot{Q}_k t_s \tag{5.2.4}$$

which however requires sampling times much shorter than the actual process timescale to be accurate.

A more refined algorithm for computing Q_k that works if the matrix A_k does not contain zero-valued eigenvalues is described in [48][2] and is presented in 5.1.

The routine for solving the continuous-time Lyapunov equation is commonly found in scientific computing environments, therefore its implementation in the code is relatively straightforward.

[2]The same paper also provides a solution for systems with integrators.

The increased computation time of this solution compared to the crude discretization is offset by the possibility of increasing the estimator step size with no significant loss of accuracy.

5.3 Selection of the corrected set

As it was shown in section 5.1, the system to be estimated is globally not observable, and some states contribute to unobservability more than others. While it is still possible to perform state estimation on such a system (as long as the system is detectable, the DARE 2.4.48 admits a stable solution), trying to correct the whole set of states could lead to failures due to numerical errors. One possibility to circumvent this problem is to limit the correction step to only those states that are most observable.

In order not to load the notation too much, the time instance subscript k is dropped in this section.

From a mathematical point of view the idea is to find the permutation matrix M that makes possible to express the state vector x as:

$$\bar{x} = \begin{pmatrix} x_c \\ x_s \end{pmatrix} = Mx \tag{5.3.1}$$

where x_c is the vector of states to be corrected and x_s the vector of states to be just simulated.

The elements of F, H, P and Q are also rearranged so that

$$\bar{F} = \begin{pmatrix} F_c & F_{cs} \\ F_{sc} & F_s \end{pmatrix} = MFM^T \tag{5.3.2}$$

$$\bar{H} = \begin{pmatrix} H_c & H_s \end{pmatrix} = HM^T \tag{5.3.3}$$

$$\bar{P} = \begin{pmatrix} P_c & P_{cs} \\ P_{cs}^T & P_s \end{pmatrix} = MPM^T \tag{5.3.4}$$

$$\bar{Q} = \begin{pmatrix} Q_c & Q_{cs} \\ Q_{cs}^T & Q_s \end{pmatrix} = MQM^T \tag{5.3.5}$$

The prediction step of the Kalman filter is left substantially unchanged, and in particular the error covariance propagation is written as:

$$\bar{P}^- = \bar{F}\bar{P}^+\bar{F}^T + \bar{Q} \tag{5.3.6}$$

The correction step, instead, is performed only on the portions x_c and P_{cc}:

$$K_c = P_c^- H_c^T (H_c P_c^- H_c^T + R)^{-1} \tag{5.3.7}$$
$$x_c^+ = x_c^- + K_c r \tag{5.3.8}$$
$$P_c^+ = (I - K_c H_c) P_c^- \tag{5.3.9}$$

The stability of this configuration can be discussed by expanding the steady state covariance equation:

$$\begin{pmatrix} P_c & P_{cs} \\ P_{cs}^T & P_s \end{pmatrix} = \begin{pmatrix} F_c & F_{cs} \\ F_{sc} & F_s \end{pmatrix} \begin{pmatrix} P_c^+ & P_{cs} \\ P_{cs}^T & P_s \end{pmatrix} \begin{pmatrix} F_c & F_{cs} \\ F_{sc} & F_s \end{pmatrix}^T + \begin{pmatrix} Q_c & Q_{cs} \\ Q_{cs}^T & Q_s \end{pmatrix} \tag{5.3.10}$$

with

$$P_c^+ = P_c - P_c H_c^T (H_c P_c H_c^T + R)^{-1} H_c P_c \tag{5.3.11}$$

Eq. 5.3.10 can be written as a system of four matrix equations:

$$P_c = F_c P_c^+ F_c + F_{cs} P_{cs}^T F_c^T + F_c P_{cs} F_{cs}^T + F_{cs} P_s F_{cs}^T + Q_c \tag{5.3.12}$$
$$P_{cs} = F_c P_c^+ F_{sc}^T + F_{cs} P_{cs}^T F_{sc}^T + F_c P_{cs} F_s^T + F_{cs} P_s F_s^T + Q_{cs} \tag{5.3.13}$$
$$P_s = F_{sc} P_c^+ F_{sc}^T + F_s P_{cs} F_{sc}^T + F_{sc} P_{cs} F_s^T + F_s P_s F_s^T + Q_s \tag{5.3.14}$$
$$P_c^+ = P_c + P_c H_c^T (H P_c H^T + R)^{-1} H P_c \tag{5.3.15}$$

It should be noted that equations 5.3.12 and 5.3.15 can be combined to form a DARE in P_c, that admits a positive definite solution as long as (F_c, H_c) is detectable and $F_{cs} P_{cs}^T F_c^T + F_c P_{cs} F_{cs}^T + F_{cs} P_s F_{cs}^T$ symmetric (which can be easily demonstrated).

Equation 5.3.14 is a discrete Lyapunov equation in P_s that admits a positive definite solution if F_s is asymptotically stable and $F_{sc} P_c^+ F_{sc}^T + F_s P_{cs} F_{sc}^T + F_{sc} P_{cs} F_s^T + Q_s$ is symmetric (which can be easily demonstrated).

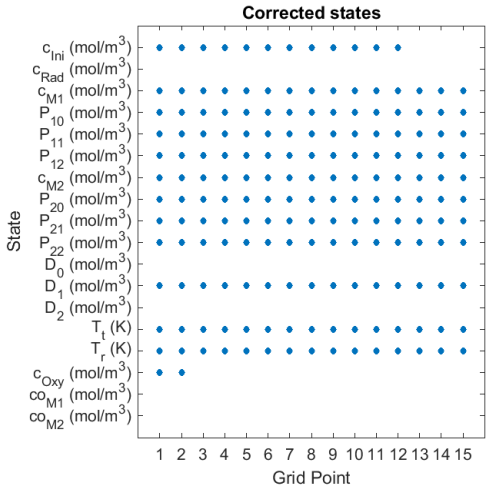

Figure 5.5: Corrected set

Equation 5.3.13 can be thought of as a linear system in the elements of P_{cs} and admits a solution if the corresponding coefficient matrix is full rank[3].

These clues suggest that if the full system admits a stable solution for the steady state covariance, a stable solution should exist also for the reduced order system if the linear system resulting from 5.3.13 can be proven to be full rank.

The choice of the corrected set can be motivated by the analysis of section 5.1: one could, for example, choose to correct only those states with an unobservability index lower than some tolerance. The oxygen and radical states, for example, are almost completely unobservable and can be only simulated, together with the dead polymer zeroth and second moment.

The choice of the corrected set for the plant is presented in table 5.5, where the elements of the corrected set are marked with an dot.

[3]The matrix equality

$$X = A_1 X A_2 + A_3 X^T A_4 + B$$

with $X \in \mathbb{R}^{m \times n}$ and A_1, A_2, A_3, A_4 and B matrices of appropriate sizes, can be rewritten as:

$$X_{ij} - \sum_{k=1}^{m} \sum_{l=1}^{n} (A_{1,ik} \cdot A_{2,lj} + A_{3,il} \cdot A_{4,kj}) \cdot X_{kl} = B_{ij}$$

which is linear in the elements of X.

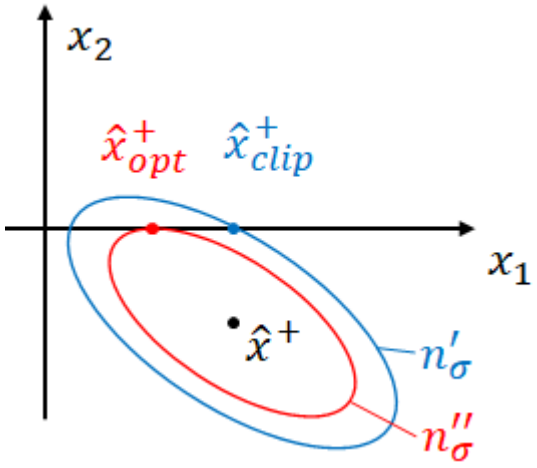

Figure 5.6: Loss of optimality due to clipping in the corrected state estimate [50]

5.4 Correction of the nonphysical state estimates

Due to the fact that the EKF has no physical knowledge of the process, it's possible that nonphysical states result from the correction step, such as negative concentrations. This can cause problems to the predictor integrator and should be avoided.

One possibility is to clip negative states to zero after correction. This computationally inexpensive trick comes with its drawbacks: in case clipping occurs, the state estimate is no longer optimal.

This effect is illustrated in figure 5.6 for the case of two variables. The black dot represents the corrected (*a posteriori*) state estimate $\hat{x}^+$ with error covariance P^+, which has a negative component that is physically meaningless. Clipping the negative state to zero lands the new state estimate to $\hat{x}^+_{clip}$, which belongs to an ellipse of constant uncertainty n'_σ. Clearly, for the same error distribution, it is possible to find an ellipse of constant uncertainty $n''_\sigma < n'_\sigma$ that is centered on $\hat{x}^+$, and tangent to the axis x_1. The tangence point $\hat{x}^+_{opt}$ is the optimal constrained state estimate.

Optimal constrained implementations of the Kalman filter exist, but they usually employ least squares optimization over the state vector. This route is not viable for a system of 270 states. A simpler algorithm was adapted from [50] that finds a near optimal solution for box constraints and is presented in

Algorithm 5.2 Correction algorithm for negative states [50]

1. Compute $\hat{x}_k^+$ and P_k^+ according to the previous equations;
2. Initialize the empty set $\mathbb{A}_c$ of clipped states and the vector $\hat{x}_c = \hat{x}_k^+$;
3. Define the set $\mathbb{A}_n$ as the ordered set of negative states in $\hat{x}_c$. Replace the corresponding values with 0 in $\hat{x}_c$;
4. Update $\mathbb{A}_c = \mathbb{A}_c \cup \mathbb{A}_n$;
5. Define the set $\mathbb{A}_u$ as the ordered set of states not included in $\mathbb{A}_c$;
6. Update the states of x_c in the ordered set $\mathbb{A}_u$:

$$\hat{x}_{c,\mathbb{A}_u} = \hat{x}_{c,\mathbb{A}_u} + P^+_{k\mathbb{A}_u\mathbb{A}_c} \left(P^+_{k\mathbb{A}_c\mathbb{A}_c}\right)^{-1} \left(\hat{x}_{c,\mathbb{A}_c} - \hat{x}^+_{k,\mathbb{A}_c}\right) \tag{5.4.1}$$

7. Repeat steps $3 \rightarrow 6$ until the ordered set $\mathbb{A}_c$ becomes empty.

algorithm 5.2.

5.5 Tuning procedure for the extended Kalman filter

Very often in literature, the tuning procedure for the Kalman filter is described as a trial and error process based more on the experience of the practitioner than on theoretically sound procedures. Moreover, most of the times, the Q matrix is built as a constant diagonal matrix, as the exact nature of the process noise is unknown [44].

After a cospicuous number of unsuccessful simulations and Kalman filter failures, it became clear that a well defined procedure for tuning the EKF was required both to save time and to obtain consistent results.

One possibility, suggested by literature [41, 46], is to determine the noise statistics of the EKF from readily available data and is described in the following sections.

5.5.1 Tuning of the R matrix

The $R \in \mathbb{R}^{m \times m}$ matrix (measurement noise covariance) can be easily determined from the knowledge of the noise pickup characteristics of the sensing elements used. One widely accepted method is to construct a diagonal matrix

$$\Sigma = \begin{pmatrix} \sigma_1 & 0 & \dots & 0 \\ 0 & \sigma_2 & & 0 \\ \vdots & & \ddots & \vdots \\ 0 & 0 & \dots & \sigma_m \end{pmatrix} \tag{5.5.1}$$

with the element σ_i equal to the standard deviation of the noise for i-th the measurement. The noise covariance matrix can then be computed as:

$$R = k_R \Sigma^2 \tag{5.5.2}$$

where k_R is a scalar tuning parameter that can be used to tweak estimator performance. Increasing k_R decreases the EKF sensitivity to measurements, making its behaviour closer to the one of an open loop state estimator (slower and smoother), while decreasing it results in a more aggressive correction.

5.5.2 Adaptive tuning of the Q matrix

Tuning of the $\dot{Q}$ matrix is the trickiest part of the whole EKF tuning procedure. A common practice is to set $\dot{Q}$ to a fixed diagonal matrix, whose elements are chosen by trial and error. This modality, unfortunately, is very labour intensive and only applicable to small systems, not to mention the fact that it inherently leads to suboptimal EKF configurations, as it completely disregards the off diagonal elements. Literature suggests, however, that if a more sound tuning procedure is used, the EKF performance can be significantly improved (to the point that it becomes comparable to more advanced state estimators) and the effort for tuning the estimator reduced to the minimum [41, 46].

Let the system be described by:

$$\dot{x} = f(x, u, p) \tag{5.5.3}$$

where p denotes a vector of time-varying random parameters that result from the effect of unmeasured disturbances and structural model error. The nominal value of these parameters $\bar{p}$ is then determined by fitting a number of experiments.

The model implemented in the EKF will make use of the nominal parameter vector:

$$\dot{x} = f(x, u, \bar{p}) + \dot{w} \tag{5.5.4}$$

$$\dot{w} \sim \mathcal{N}(0, \dot{Q}) \tag{5.5.5}$$

If we define the parameter vector as the sum of the nominal value plus a normally distributed zero mean stochastic term of covariance C_p [41, 46]

$$p = \bar{p} + \delta p \tag{5.5.6}$$

$$\delta p \sim \mathcal{N}(0, C_p) \tag{5.5.7}$$

we can then approximate the effect of parameter variation in the system equation through a Taylor expansion:

$$\dot{x} \simeq f(\hat{x}, u, \bar{p}) + J_{f,p}\delta p \tag{5.5.8}$$

where $J_{f,p}$ is the jacobian of the model function with the respect to the parameter vector:

$$(J_{f,p})_{i,j} = \left(\frac{\partial f_i}{\partial p_j}\right)_{\hat{x},u,\bar{p}} \tag{5.5.9}$$

If we set the process noise term in the model function to be equal to $J_{f,p}\delta p$, we can then compute the covariance matrix $\dot{Q}$ as [41, 46]:

$$\dot{Q} = J_{f,p} C_p J_{f,p}^T \tag{5.5.10}$$

The determination of C_p is a problem in and of itself, but it can be approached on physical grounds by looking at how parameters were fitted in the first place. One possibility, if confidence intervals are provided, would be to set the diagonal elements of C_p to the square of the confidence interval width. Alternatively, if $\bar{p}$ was fitted via least squares methods, it is possible to approximate C_p^{-1} with

the Hessian matrix of the cost function[4] [4].

The advantage of this formulation is that it allows to direct the action of the Kalman filter towards those states that are most affected by parametric uncertainty. Additionally, just as it was done for the tuning of the R matrix, it is possible to introduce the tuning parameter k_Q for tweaking the response of the filter:

$$\dot{Q} = k_Q J_{f,p} C_p J_{f,p}^T \tag{5.5.11}$$

5.6 Initialization of the filter

A correct initialization of the EKF can be crucial to its transient behaviour, however it is implicit in the nature of the filter that some level of uncertainty in the initial state estimate is tolerated if the initial error covariance is chosen knowingly. A poor initialization of the error covariance can lead the EKF to fail in multiple ways. For example, if P_0 is chosen too small the filter will perform sluggishly at best and will "learn" the wrong estimate too well, with the possibility of not being able to settle to the correct state estimate at all. If, conversely, P_0 is chosen too big, the filter will react erratically with plenty of oscillations and the possibility of diverging uncontrollably.

One very practical way to initialize the state estimate $\hat{x}$ is to set it to the steady state value x_{ss} corresponding to the current control input u.

The initial error covariance P_0 should be chosen to reflect the uncertainty in the initial estimate. This is practically impossible to determine rigorously, however if lower and upper bounds are available for the state variables (x_{upper}, x_{lower}), it is possible to define a mean state vector

$$x_m = \frac{x_{upper} + x_{lower}}{2} \tag{5.6.1}$$

and then to construct P_0 as a diagonal matrix with the element $P_{0,i} = (\hat{x}_{0,i} - x_{m,i})^2$ [41].

If the estimator is initialized at a steady state and the plant is stable in such steady state, one possibility is to compute the solution of the discrete Lyapunov

[4]The Hessian matrix is very often provided as an output argument in optimization routines in scientific numerical packages

equation:

$$X = FXF^T + Q \tag{5.6.2}$$

with F and Q computed at the steady state, and set P_0 as:

$$P_0 = k_P X \tag{5.6.3}$$

with k_P an additional tuning parameter to adjust the confidence in the initial estimate and to tweak the initial response.

5.7 Scaling of the process variables and statistics

Due to the fact that the states to be estimated span very different numeric ranges, the jacobians that result from the linearization of the system can become very poorly conditioned very quickly, especially for system of important size, leading to problems when computing F, not to mention the fact that numerically integrating a badly scaled function during the prediction step is not guaranteed to yield meaningful results.

In order to cope with these issues, the process variables and statistics are unscaled using the diagonal scaling matrices $X_{sc} \in \mathbb{R}^{m \times m}$ and $Y_{sc} \in \mathbb{R}^{n \times n}$, defined as:

$$X_{sc} = \text{diag}\left(x_{1,sc}, x_{2,sc}, \ldots, x_{m,sc}\right) \tag{5.7.1}$$

$$Y_{sc} = \text{diag}\left(y_{1,sc}, y_{2,sc}, \ldots, y_{n,sc}\right) \tag{5.7.2}$$

The Kalman filter will operate on the unscaled variables x^* and y^* defined as:

$$x^* = X_{sc}^{-1} x \tag{5.7.3}$$

$$y^* = Y_{sc}^{-1} y \tag{5.7.4}$$

The model and output functions are rewritten in terms of x^*, $\dot{x}^*$ and y^*, resulting in the unscaled jacobians:

$$A^* = X_{sc}^{-1} A X_{sc} \tag{5.7.5}$$

$$H^* = Y_{sc}^{-1} H X_{sc} \tag{5.7.6}$$

The unscaled state transition matrix F^* is computed using the methods presented in the previous sections on A^*.

The noise statistics must also be unscaled:

$$\dot{Q}^* = X_{sc}^{-1} \dot{Q} X_{sc}^{-1} \tag{5.7.7}$$

$$R^* = Y_{sc}^{-1} R Y_{sc}^{-1} \tag{5.7.8}$$

The choice of X_{sc} and Y_{sc} is more or less arbitrary, as long as it results in a better conditioning of the jacobians. It was found, however, that scaling with respect to the ranges of variation of the variables led to better results than scaling with respect to absolute values.

A procedure to automate the generation of the scaling matrices was tried with success during this work and is described in algorithm 5.3.

5.8 Performance evaluation of the estimator

In order to characterize the performance of the estimator, a number of indicators can be defined to measure the quality of the estimation.

5.8.1 State error

One very natural measure for the state estimator performance is the relative error between the state estimate and the real state:

$$e(t, z) = \frac{\hat{x}(t, z) - x(t, z)}{x(t, z)} \tag{5.8.1}$$

where the division is performed element-wise, since $x(t, z)$ is a vector.

If we are not interested in the sign of the error, we can take the absolute value $|e|$ and define a number of useful functions, such as the cumulative maximum of the error:

$$|e|_{max}(t, z) = \max_{t' \in [t; +\infty]} |e(t', z)| \tag{5.8.2}$$

Algorithm 5.3 Automatic generation of scaling matrices

1. simulate an input step response of the system. The choice of the step size is arbitrary, as long as it is realistic for the process. The duration of the simulation N_s should be enough for the system to reach steady state.

2. create the sample matrices X and Y as:

$$X = \begin{pmatrix} x_1^T \\ x_2^T \\ \vdots \\ x_{N_s}^T \end{pmatrix} \tag{5.7.9}$$

$$Y = \begin{pmatrix} h(x_1)^T \\ h(x_2)^T \\ \vdots \\ h(x_{N_s})^T \end{pmatrix} \tag{5.7.10}$$

3. compute $\bar{x}$ and $\bar{y}$ as the sample averages of X and Y:

$$\bar{x}^T = \frac{1}{N_s} \sum_{k=1}^{N_s} X_k \tag{5.7.11}$$

$$\bar{y}^T = \frac{1}{N_s} \sum_{k=1}^{N_s} Y_k \tag{5.7.12}$$

4. compute the scaling matrices X_{sc} and Y_{sc} as:

$$\mathrm{diag}(X_{sc}) = \mathrm{diag}\left(\sqrt{\frac{1}{N_s - 1} \sum_{k=1}^{N_s} \left(X_k - \bar{x}^T\right)^T \left(X_k - \bar{x}^T\right)} \right) \tag{5.7.13}$$

$$\mathrm{diag}(Y_{sc}) = \mathrm{diag}\left(\sqrt{\frac{1}{N_s - 1} \sum_{k=1}^{N_s} \left(Y_k - \bar{y}^T\right)^T \left(Y_k - \bar{y}^T\right)} \right) \tag{5.7.14}$$

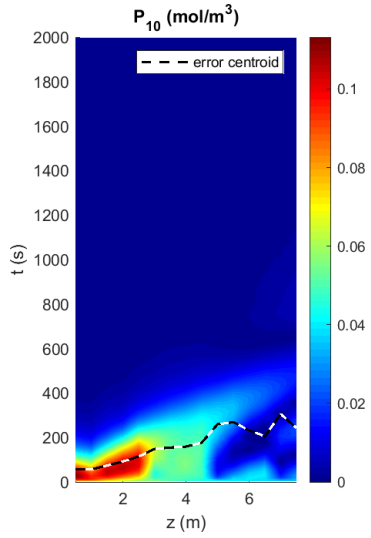

Figure 5.7: Relative error heat map

Because the state of the plant is a function of both time and position along the reactor axis, $|e|$ and $|e|_{max}$ can be represented either by holding one variable still or by the means of heat maps or contour plots.

Heat maps are extremely helpful and intuitive in studying the propagation of the error inside the system, although they fail to convey quantitative informations. An example is given in figure 5.7, that shows the evolution of error in the zeroth moments in an initialization simulation.

Drawing the contour plot for $|e|_{max}$ gives precise information about the error settling time, as it is shown in figure 5.8 for the same simulation as before.

If we treat e^2 as a distribution, we can reduce its size by defining its $k-$th moment:

$$\mu_k(z) = \int_0^{t_f} t^k e(t,z)^2 dt \tag{5.8.3}$$

For $k = 0$ we can define the integral squared error as the zeroth moment, giving a measure of the total mass of the estimation error:

$$\text{ISE}(z) = \mu_0(z) = \int_0^{t_f} e(t,z)^2 dt \tag{5.8.4}$$

It is also possible to define the error centroid as the ratio between the first error moment and the zeroth error moment, representing the center of mass of

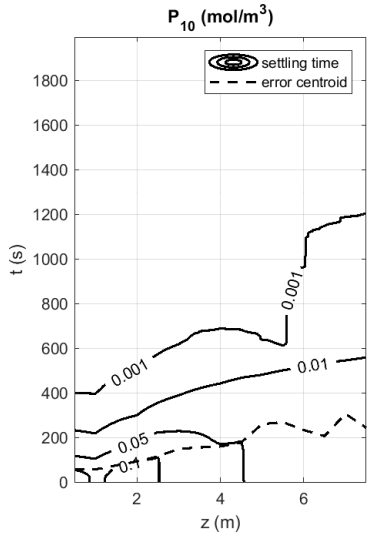

Figure 5.8: Settling time contour plot

the estimation error:

$$\bar{t}(z) = \frac{\mu_1(z)}{\mu_0(z)} \tag{5.8.5}$$

5.8.2 Output error

While the presented approaches based on the state estimation error are very natural in theory, their applicability is questionable in practice for several reasons: first of all, the true state variables are unknown, making these tools relevant in simulations only. Furthermore, the bigger the model is in terms of states, the more cumbersome these tools get.

The measurement residual, defined as:

$$r_k = y_k - h(\hat{x}_k^-, u_{k-1}) \tag{5.8.6}$$

is the difference between the measurement vector and the predicted output according to the previous state estimate. If the EKF has converged to the correct state estimate, the residual is expected to fall in the order of magnitude of the measurement noise standard deviation.

It is possible to define a scalar index that summarizes this information:

$$\alpha = \sqrt{r^T \Sigma^{-2} r} \tag{5.8.7}$$

If the prediction is in agree with the measurement, $\alpha \to 1$. On the other hand, a value of α much greater than 1 would indicate a very poor state estimate.

5.9 EKF performance in simulations

A number of computer simulations are presented here to demonstrate the performance of the Kalman filter and the effect of the various tuning parameters. Two scenarios were envisioned for this purpose: an initialization with state mismatch due to previous (unspecified) dynamics and a steady state initialization with parameteric mismatch.

The nominal parameter vector $\bar{p}$ and the parameter covariance matrix C_p for computing the Q matrix were provided from the previous fitting of the model [42]. The coefficients of the pressure drop model were fitted from [16], but they are likely to be incorrect and should have been verified by experimental work.

5.9.1 Initialization with state mismatch

An input flowrate of $u_0 = 0.4\ kg/h$ is chosen for the simulation. The state estimator is tuned using the procedures described in the previous sections to the steady state of the system $\hat{x}_0^+ = x_{ss}(u_0)$. The initial covariance of the estimation error is computed using the solution of the Lyapunov equation.

The system simulation is initialized to the same steady state plus a 2% deviation on the reactor temperature states:

$$x_0 = x_{ss}(u_0) + \delta x_{T_r}(2\%) \tag{5.9.1}$$

For example, a 2% deviation on a temperature of 333K (60 °C) would amount to 6.66 K.

The effect of this deviation on the system is quite drastic, as it induces an overall increase in reaction rates that results in the rising of both the number of polymer chains and average chain lengths.

For making comparisons, WACL is used as reference (at 2.5 m and 7.5 m, where temperature is not measured), as it reflects the quality of the polymer and determines one of the most critical safety indicators. Other state variables,

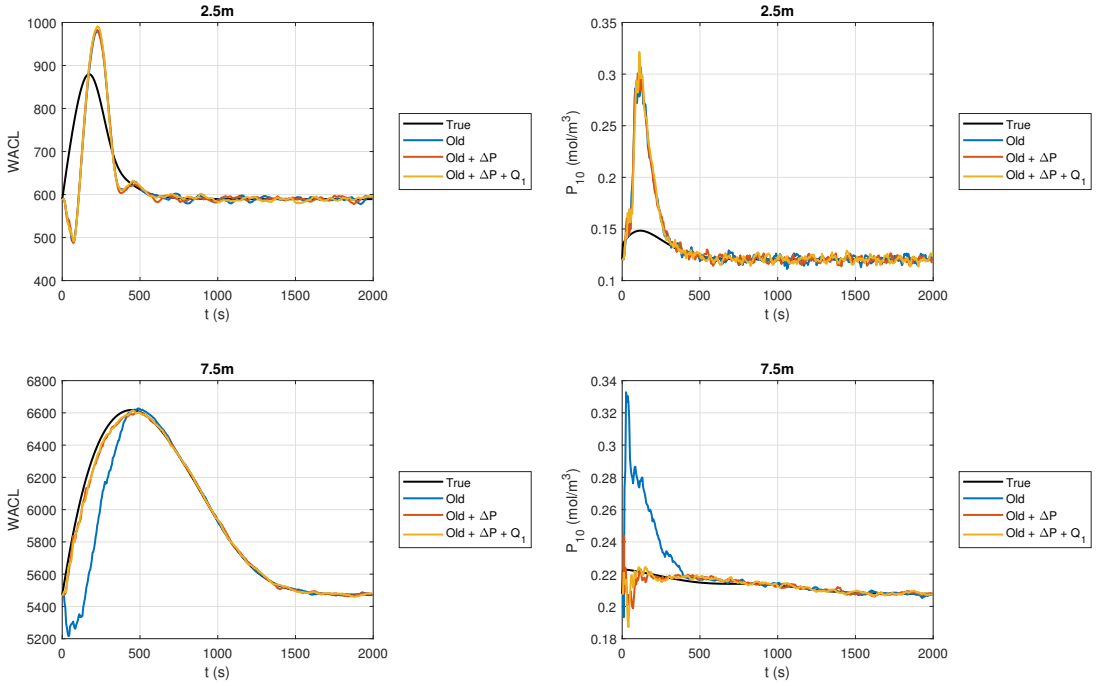

(a) Effect on WACL (b) Effect on AAM active chain zeroth moment

Figure 5.9: Effect of the measured set in initial state mismatch simulation

such as the zeroth, first and second moment of the AAM active polymer chain, the AAM concentration and the reactor temperatures are shown in the same grid points.

First, the improvement between the old measured set and the new configuration with the DP cell added is demonstrated. Then, various tuning configurations will be explored and the results discussed.

Effect of the measured set

The effect of the measured set is tested for the tuning: $k_R = 1$, $k_Q = 1$, $k_P = 1$ and shown in figures **??** a−b for WACL and the zeroth moment of the AAM active chain. From these plots it is possible to see a clear improvement in the rate of convergence of the estimate when the pressure drop measurement is added.

The first moment constraint described in section 4.3.4 does not appear to have an effect on the rate of convergence, however it can be shown to slightly limit the monomers mass balance violation, as it is presented in figure 5.10.

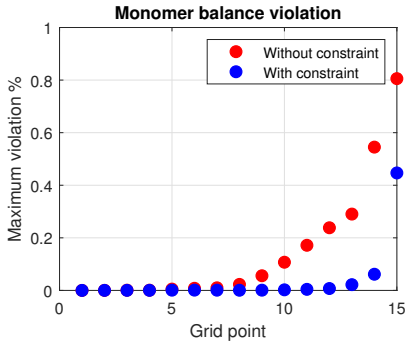

Figure 5.10: Effect of the measured set on the monomer balance violation in initial state mismatch simulation

It is possible to have a clearer picture of which states are most affected by the newly added measurements by representing the relative error distribution in time and space on a heat map. In figures 5.11 a−b, the error propagation in the zeroth moment states is shown for the old configuration and for the new one (with the first moment constraint added). The difference between the two is not striking, however it should be noted that the information made available by the new measurements only results in a faster correction of the states near the outlet of the reactor. It is also interesting to see the difference between the error distribution in a state that is not observable (the zeroth moment of the dead polymer chains), which propagates along the reactor by convection and diffusion (the residence time for the current flowrate is 547 s), and the distribution in states that are observable, where the propagation is countered by correction.

Effect of k_P

The initial confidence in the state estimate of the EKF can be tweaked by increasing or decreasing k_P. The effect of k_P at constant $k_R = k_Q = 1$ is shown in figure 5.12 for WACL and the moments of the AAM active chain. In the figure it is possible to see how the behaviour of the estimator becomes more and more aggressive as k_P is increased. Values of $k_P > 10$ were found to destabilize the estimator, while $k_P = 0.1$ seemed a good compromise between aggressiveness and rate of convergence.

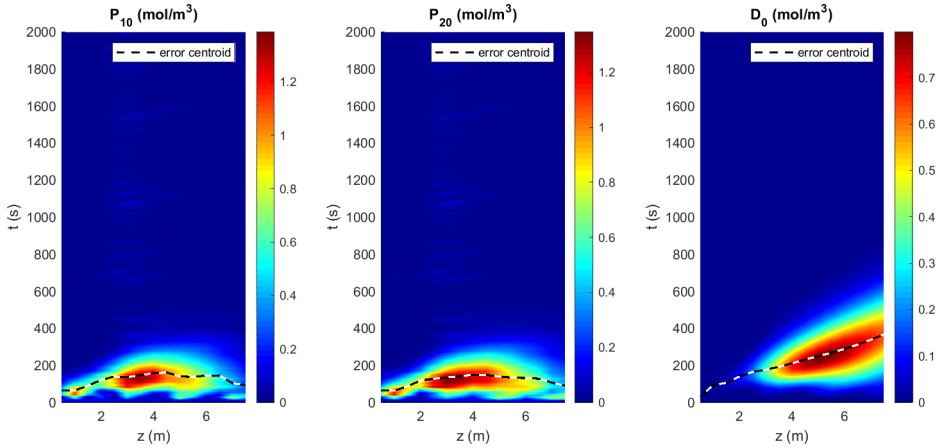

(a) Error distribution of the zeroth moments in the old configuration

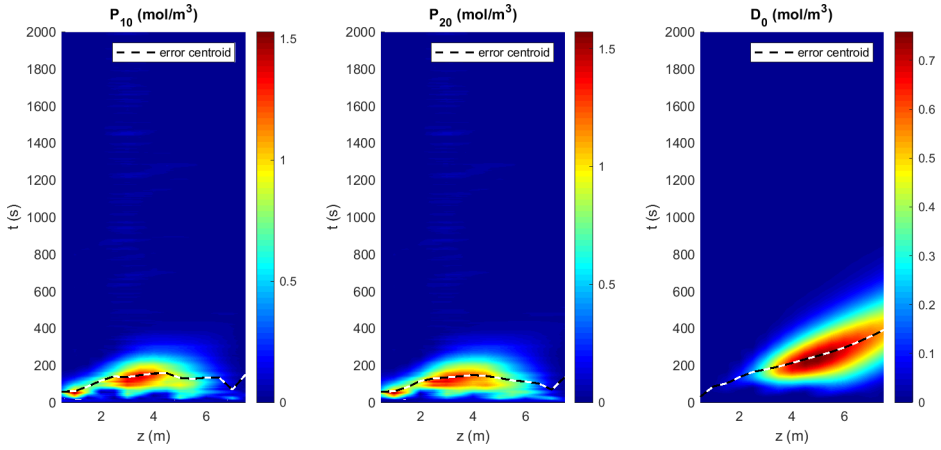

(b) Error distribution of the zeroth moments with the new measurements added

Figure 5.11: Error distribution in time and space in inital state mismatch simulation

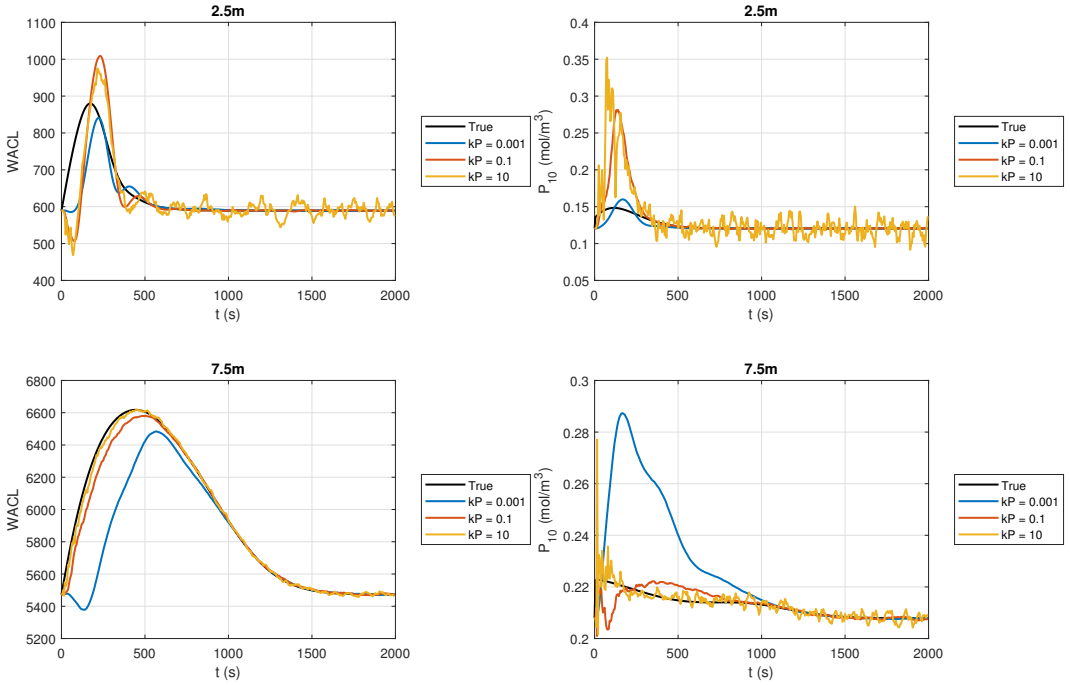

(a) Effect on WACL (b) Effect on AAM active chain zeroth moment

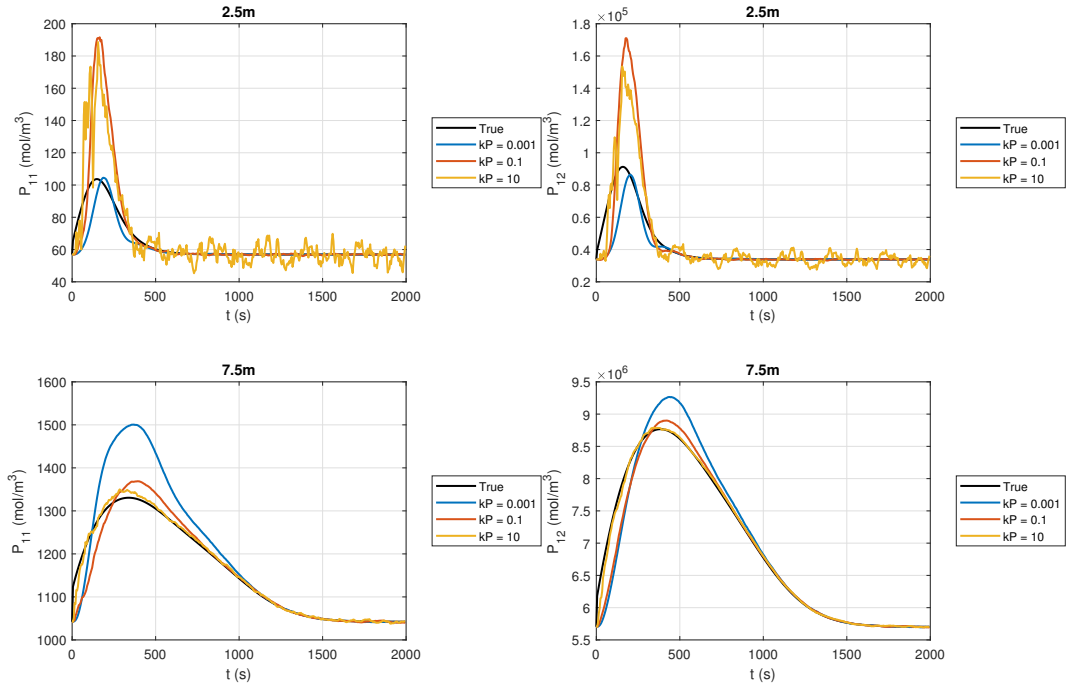

(c) Effect on AAM active chain zeroth moment (d) Effect on AAM active chain zeroth moment

Figure 5.12: Effect of k_P in initial state mismatch simulation

Effect of the tuning

Another possibility to tweak the response of the EKF is to manipulate k_R and k_Q. The estimator can be made more sensitive to measurements either by decreasing k_R or by increasing k_Q, and vice versa. In both cases the final result is to change the ratio between the projected *a priori* error covariance and the measurement error covariance (see figure 2.4 in section 2.4.5).

The effect of k_R is demonstrated in figure 5.13 at constant $k_Q = 1$, $k_P = 0.01$ for WACL and the moments of the AAM active chain.

The ISE and error centroid introduced in section 5.8 can be used to summarize the effect of different values of k_R at different grid points. In figures 5.14 a−d the two informations are combined in a scatter plot for different state variables, with the ISE coded with the size of the bubbles. Two remarks can be made: first of all, using a smaller k_R typically results in a lower centroid, meaning that the higher the gain of the observer, the earlier the error occurs. Despite the positive effect on the error centroid, however, a more aggressive tuning can negatively affect the integral squared error, especially in those states that are more "distant" from the measurement.

5.9.2 Initialization with parameter mismatch

An input flowrate of $u_0 = 0.4\ kg/h$ is chosen for the simulation. The state estimator is tuned and initialized using the procedures described in the previous sections to the steady state of the system with the nominal parameter vector $\hat{x}_0^+ = x_{ss}(u_0, \bar{p})$.

The system simulation is initialized to the steady state with 20% deviation in the radical efficiency factor (see section 2.1.1).

$$x_0 = x_{ss}\left(u_0, \bar{p} + \delta p_f(20\%)\right) \tag{5.9.2}$$

The EKF was tuned in all the simulations with $k_Q = 1$, $k_R = 0.01$, $k_P = 0$. It should be stressed that such an aggressive tuning is not always possible with parametric mismatch, and in some cases, if the deviation on the parameter vector is chosen too daringly, it will result in unstable behaviour and estimator failures.

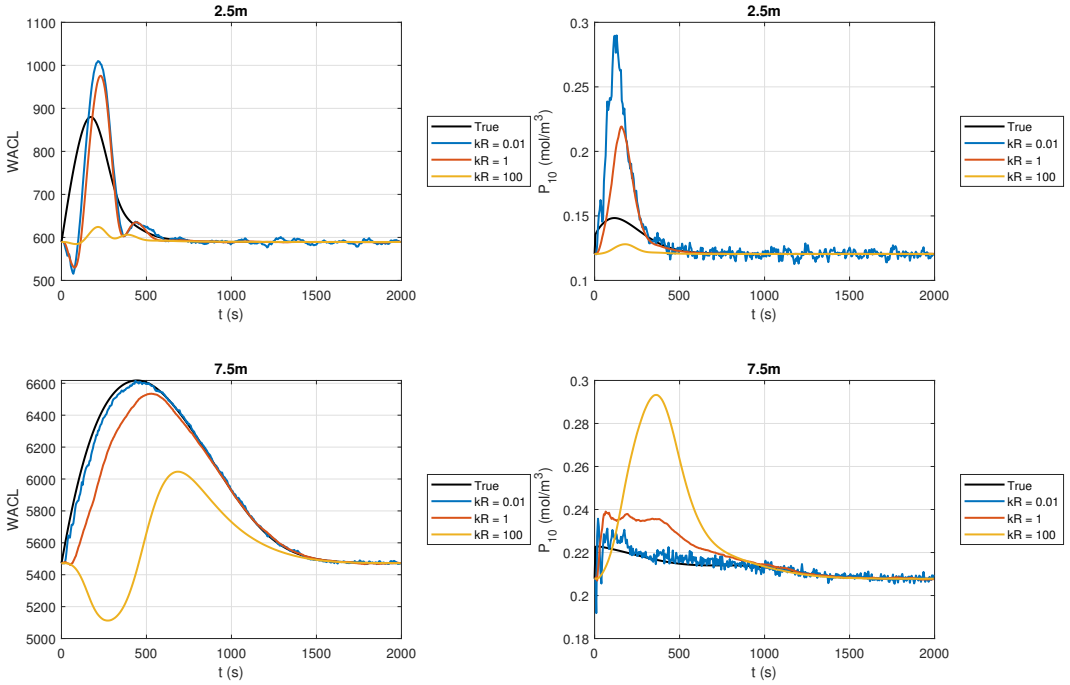

(a) Effect on WACL

(b) Effect on AAM active chain zeroth moment

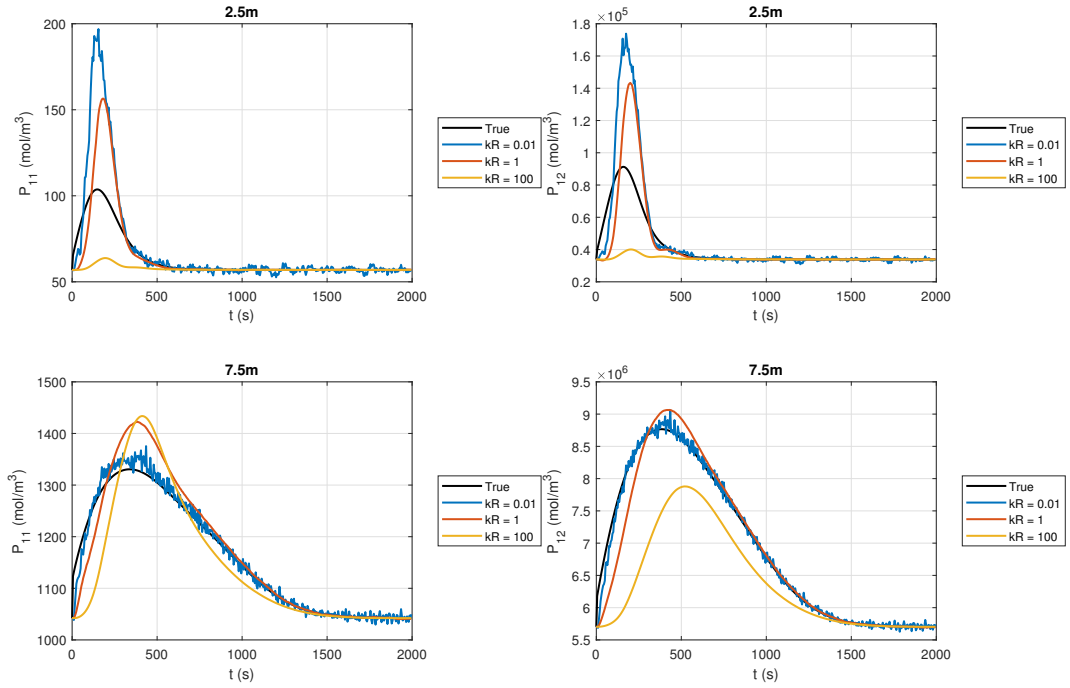

(c) Effect on AAM active chain first moment

(d) Effect on AAM active chain second moment

Figure 5.13: Effect of k_R in initial state mismatch simulation

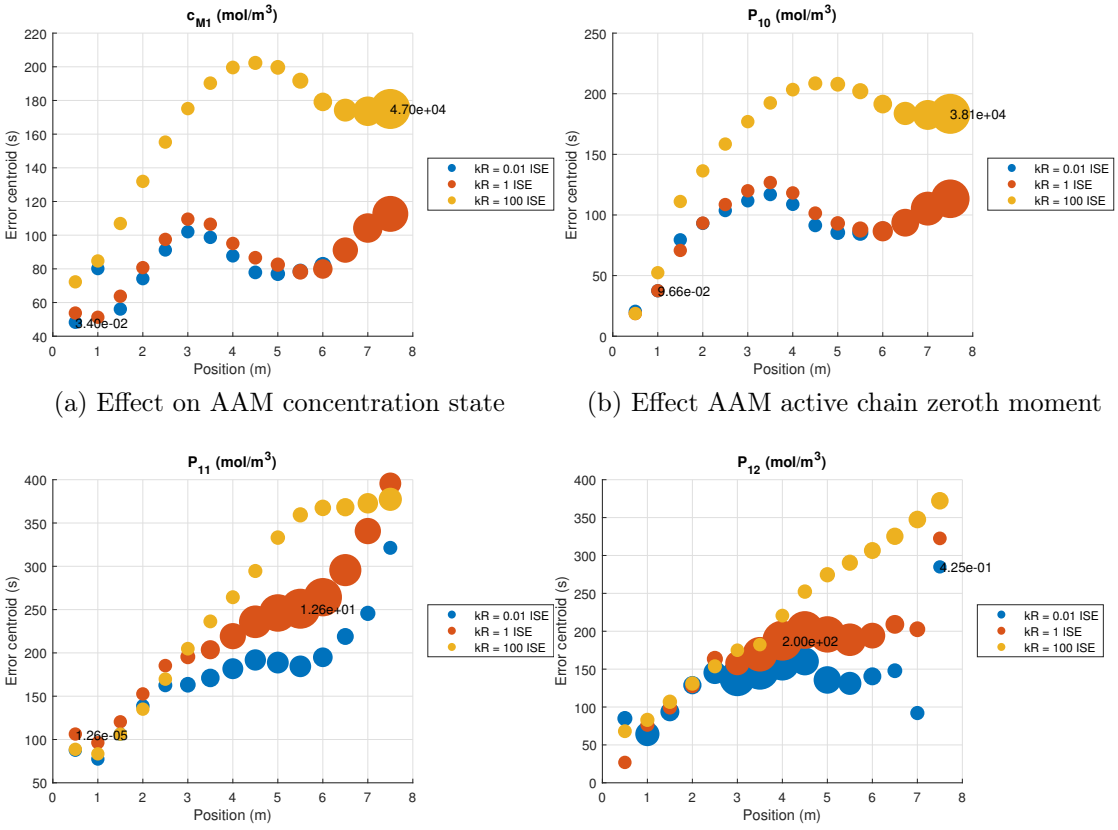

(a) Effect on AAM concentration state

(b) Effect AAM active chain zeroth moment

(c) Effect AAM active chain first moment

(d) Effect AAM active chain second moment

Figure 5.14: ISE and error centroid for different values of k_R in initial state mismatch simulation.

Effect of the measured set

The results for WACL and the moments of the AAM active chain are presented in figures 5.15 a-d. In addition to the state estimates, the output measurements and predicted outputs (*a priori*) are shown in figures 5.16 a-c. The most notable effect of the parametric mismatch is a persistent residual error in certain states and measurements that does not fully stabilize to zero. This should be expected, as the Kalman filter is derived under the assumption of zero mean noise and that parametric mismatch acts as an additional and persistent process noise component.

Just like with the case of initial state mismatch, the addition of the pressure drop measurement is beneficial to the state estimate in that it reduces the bias in the weight average chain lenght near the outlet of the reactor. However, conversely to what happens when parametric mismatch is not present, some states that are poorly observable can be steadily corrected in the wrong direction (as it can be seen in figure 5.15 c for the first moment of the AAM active polymer chain at 2.5 meters).

5.10 Estimation based on plant data

Before closing this chapter, the results from state estimation made on real plant data are presented in 5.17 and compared with the measurements.

Only the temperature and monomer concentration measurements were used with the state estimator. The state estimator was tested with both the old (fixed) Q matrix from [42] and with the new adaptive matrix. k_Q was set to 0.01 with the fixed matrix (higher values would result in estimator failures) $k_Q = 1000$ for the adaptive matrix case. $k_R = 1$ and $k_P = 1$ for both cases.

From the plots, is possible to see that both the new and the old tuning are capable of tracking the measurements in comparable and satisfactory ways, though the possibility to very quickly tune the EKF is what sets apart the proposed procedure from the previously used one.

From the AAM concentration plot it is possible to see a nonvanishing bias between the measurement and the predicted output, suggesting the presence of plant-model mismatch.

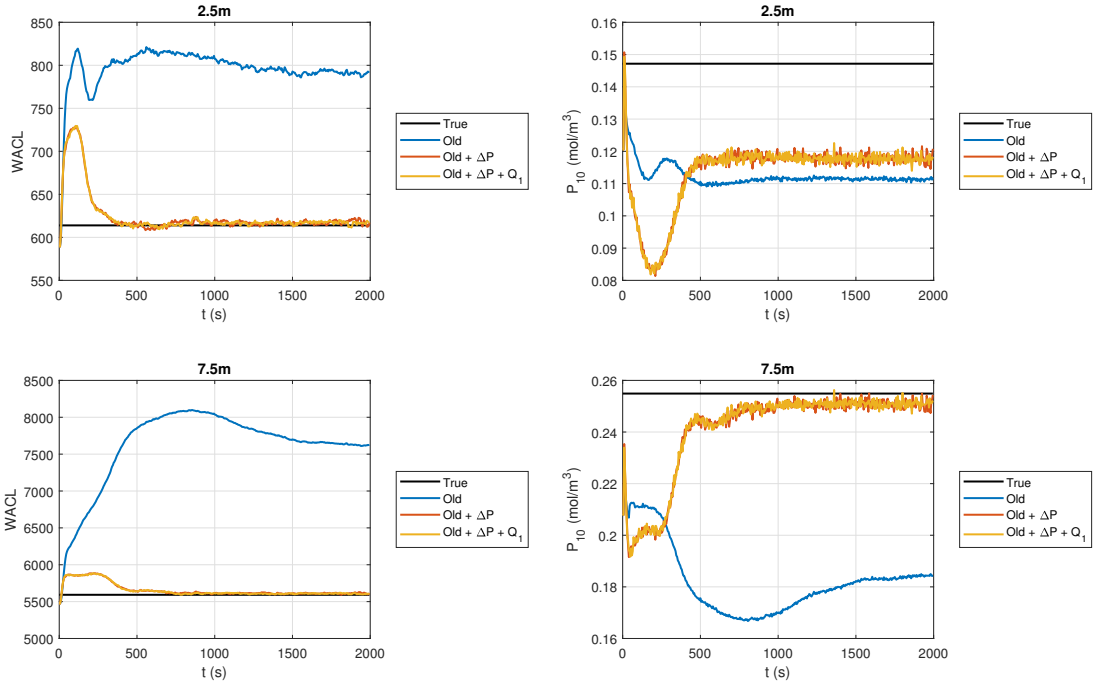

(a) Effect on WACL (b) Effect on AAM active chain zeroth moment

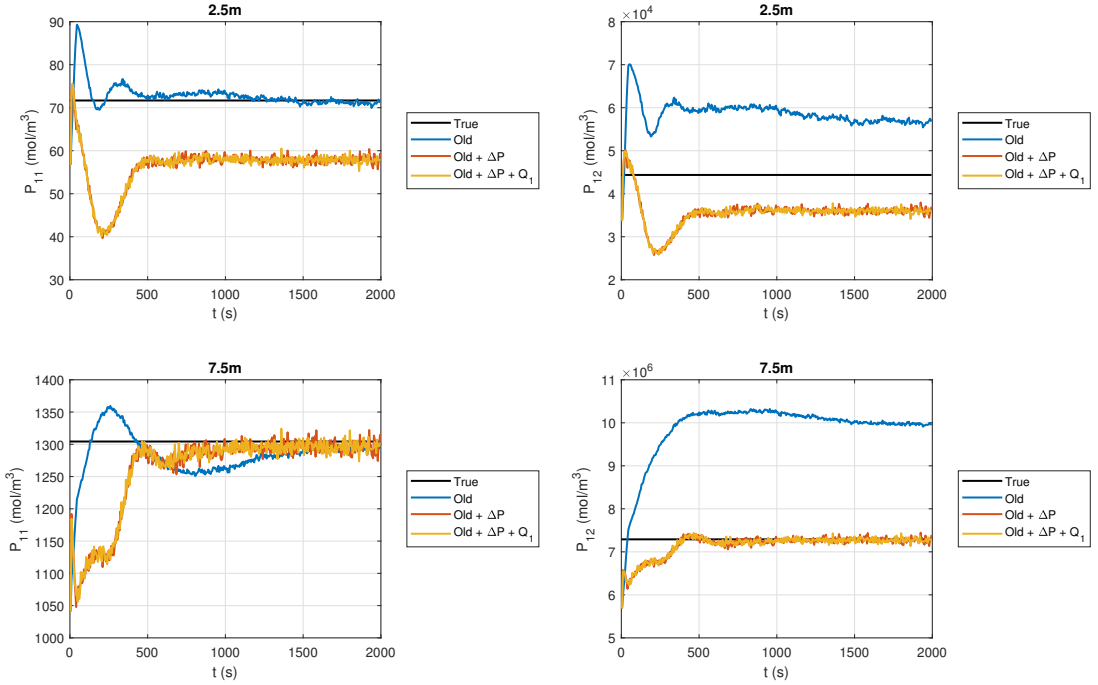

(c) Effect on AAM active chain first moment (d) Effect on AAM active chain second moment

Figure 5.15: Effect of the measured set in parameter mismatch simulation

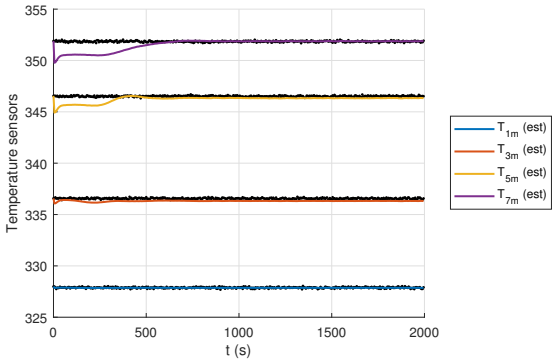

(a) Temperature measurements

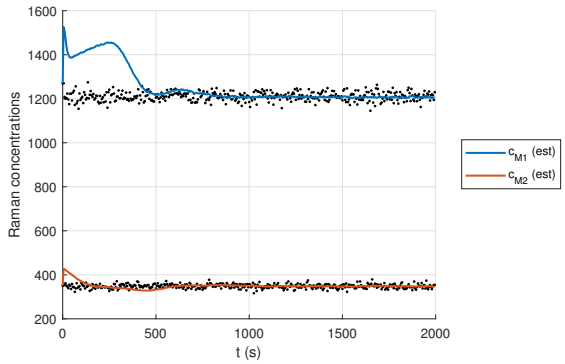

(b) Monomer concentration measurements

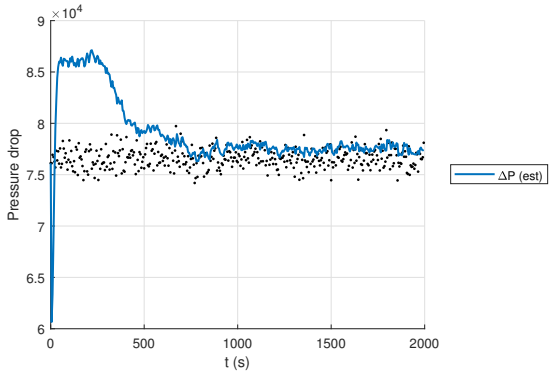

(c) Pressure drop measurement

Figure 5.16: Output bias in parameter mismatch simulation

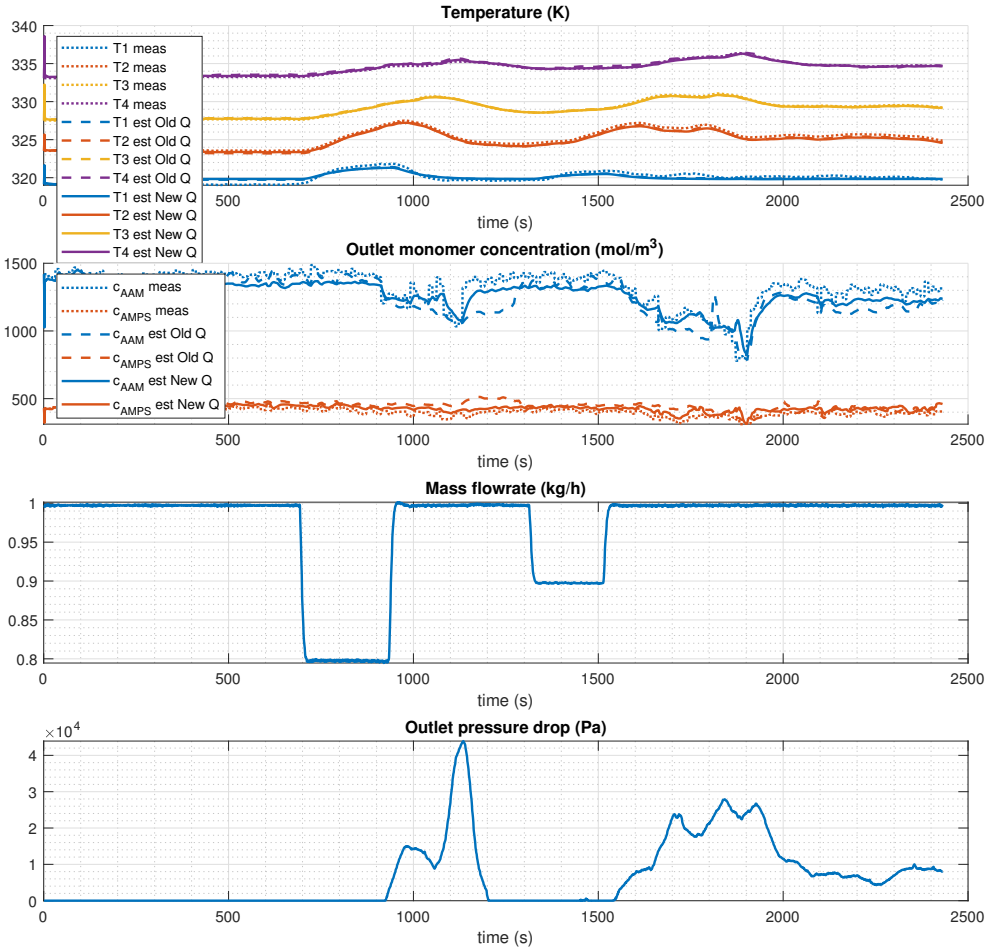

Figure 5.17: Plant data from experimental run and estimation results

Some final comments should be made regarding the measured data. The measured pressure drop, shown in the fourth plot of figure 5.17, demonstrates the sensitivity of the outlet pressure measurement to the presence of polymer and to some extent shows the effects of clogging. The presence of polymer in the outlet pipe can be deduced both by the monomer concentration measurement and the pressure drop measurement. The trend that the two curves follow, roughly speaking, is inverse: the more polymer is present in the outlet, the higher the viscosity and the lower the monomer concentration. The pressure measurement, however, is much more sensitive, especially in relation to the measurement noise, and is capable of providing the information at a higher rate than the Raman spectrometer does.

The outlet piping, however, is sensitive to fouling, due to the presence of dead zones in the fittings' junctions. The polymer can stagnate in those zones and determine clogs that distort the pressure measurement. The peaks that are visible in the fourth plot are thought to be caused by such clots. The impact of the cloggings on the reading can exceed the magnitude of the clean signal and should be considered in process development.

After the second flowrate step none of the measured variables returns to the initial baseline. This is likely caused by a combination of higher than modelled thermal inertia of the system, which in turn causes the reaction to continue for longer than the hydraulic residence time (217 s at a flowrate of 1 kg/h), and mismatch on the reaction kinetics. The increased thermal inertia of the reactor was already observed in [42] and is likely to be caused by the mass of the wooden rods used to support the reactor.

Chapter 6

Conclusion and outlook

The main objective of the thesis, the redesign of the estimator with the new pressure measurement was successfully met. The pressure sensor was installed in the plant, tested in experiments, and the influence of the polymer on the pressure reading was demonstrated. A simple model for the pressure drop was found and implemented in the code, and its beneficial effect to the state estimation problem proven in a large number of simulations.

The observability analysis that was carried out revealed that the envisioned observation scheme meets the target of providing the polymer quality information and enables a clearer view on the internal states than was possible before. Moreover, a number of tools for simplifying and systematizing the observability analysis and the observer tuning were brought together and tested with success, and in particular graph-based and indices-based observability criteria, data-based adaptive EKF tuning. These tools can be easily integrated in the NMPC framework, as they rely on readily available informations and they have the potential to ease the burden on the control engineer when designing the state estimator, with benefits in terms of better performance of the estimator itself and lower cost of the implementation.

The proposed approach for tuning the estimator relies on data that is made available by parameter estimation and instrument calibration, and allows to design the Kalman filter in a way that is consistent with its functioning principle. The more rigorous approach enables a higher flexibility of the estimator, which in turn can operate near-optimally in a number of situations potentially different from the tuning study cases.

Unobservable states are now handled in a rigorous way, by keeping track of the uncertainty propagated from and to those states. Minor improvements were also made in the areas of constrained correction and prediction step discretization. These improvements address the stability of the state estimator and allow for faster and trouble-free prototyping and simulations.

The estimator was tested in representative situations and was found to behave very satisfactorily even in presence of moderate plant-model mismatch. Improvements can still be made in the area of online parameter estimation in order to cope with parameter mismatch. What is typically done in these cases is to implement the uncertain parameters as estimated dummy states in the model and to let the Kalman filter correct them, just as it does with the actual state variables. The estimation scheme could benefit from the inlet boundary conditions being implemented as uncertain parameters.

The new equipment was tested with mixed results. Cloggings were experienced even at low conversions and it was not possible to reach steady states stable enough to fit the pressure drop model with. Additionally, it was found that the newly installed fittings constituted preferential spots for polymer clots to grow. This phenomenon can make the pressure drop measurement less reliable than anticipated and should be taken into account in future works when the pressure drop model is validated, for example by implementing the constriction of the outlet pipe as an uncertain parameter.

Further improvements in the EKF can be made by separating the prediction and correction steps and letting the observer accept a variable number of measurements. This modification is trivial in the current configuration and could open to the possibility of accepting measurements with different sampling rates in a more natural way. The Raman spectrometer, for example, produces one measurement every ten seconds and is currently upsampled by holding the measurement for ten seconds to match the sampling rate of the the temperature and pressure drop measurement, which are available once per second. This, however, introduces unnecessary delay in the measurement.

Having a flexible measurement structure could prove benefical also to reject bad measurements, such as the pressure drop readings that are distorted by cloggings, and would enable the integration of sparse, off-line measurements (such as the polymer distribution information from size exclusion chromatography

on samples of polymer collected during experimental runs) in the estimation scheme.

Bibliography

[1] Charles Alexander and Matthew Sadiku. *Fundamentals of Electric Circuits*. McGraw-Hill Education, 2012.

[2] Joel A E Andersson, Joris Gillis, Greg Horn, James B Rawlings, and Moritz Diehl. CasADi – A software framework for nonlinear optimization and optimal control. *Mathematical Programming Computation*, In Press, 2018.

[3] C. Andrade. The viscosity of liquids. *Nature*, 125(3148):309–310, mar 1930.

[4] Richard C. Aster. *Parameter Estimation and Inverse Problems*. Elsevier LTD, Oxford, 2016.

[5] Tim Babb. How a kalman filter works, in pictures. https://www.bzarg.com/p/how-a-kalman-filter-works-in-pictures/, 2015.

[6] João Carlos Alves Barata and Mahir Saleh Hussein. The moore–penrose pseudoinverse: A tutorial review of the theory. *Brazilian Journal of Physics*, 42(1-2):146–165, dec 2011.

[7] Hassager Bird, Armstrong. *Dynamics of Polymeric Liquids, Volume 1: Fluid Mechanics, 2nd Edition*. John Wiley & Sons, 1987.

[8] R. Byron Bird, Warren E. Stewart, and Edwin N. Lightfoot. *Transport Phenomena*. John Wiley & Sons Inc, 2006.

[9] Jost Brinkmann. From batch to continuous production: experimental investigation and modeling of a modular reactor concept for a continu-

ous copolymerization. Master's thesis, Technische Universität Dortmund, 2016.

[10] E. F. Camacho and C. Bordons. *Model Predictive control*. Springer London, 2007.

[11] W.R. Dean. XVI.note on the motion of fluid in a curved pipe. *The London, Edinburgh, and Dublin Philosophical Magazine and Journal of Science*, 4(20):208–223, jul 1927.

[12] Ramsey Faragher. Understanding the basis of the kalman filter via a simple and intuitive derivation [lecture notes]. *IEEE Signal Processing Magazine*, 29(5):128–132, sep 2012.

[13] Ralf Gesthuisen and Sebastian Engell. State estimation for tubular reactors with measurements at the outlet only. *IFAC Proceedings Volumes*, 33(10):935–940, jun 2000.

[14] Volker Gnielinski. G3 durchströmte rohrwendeln. In *VDI-Wärmeatlas*, pages 801–804. Springer Berlin Heidelberg, 2013.

[15] Don Green and Robert Perry. *Perry's Chemical Engineers' Handbook, Eighth Edition*. McGraw-Hill Education, 2007.

[16] Muhammad R. Hashmet, Mustafa Onur, and Isa M. Tan. Empirical correlations for viscosity of polyacrylamide solutions with the effects of concentration, molecular weight and degree of hydrolysis of polymer. *Journal of Applied Sciences*, 14(10):1000–1007, oct 2014.

[17] M. Hautus. Controllability and stabilizability of sampled systems. *IEEE Transactions on Automatic Control*, 17(4):528–531, aug 1972.

[18] Michael T. Heath. *Scientific Computing*. The McGraw-Hill Companies, Inc., 2002.

[19] J. Heemskerk, R Rosmalen, R. Janssen-van, R.J. Holtslag, and D. Teeuw. Quantification of viscoelastic effects of polyacrylamide solutions. In *SPE Enhanced Oil Recovery Symposium*. Society of Petroleum Engineers, 1984.

[20] Nicholas J. Higham. The scaling and squaring method for the matrix exponential revisited. *SIAM Journal on Matrix Analysis and Applications*, 26(4):1179–1193, jan 2005.

[21] Dong Jin-long and Mo Bo. The method of system observability analysis using pseudo-inverse of system observability matrix. *Proceedings of the 32nd Chinese Control Conference*, pages 55–59, 2013.

[22] R.E. Kalman. On the general theory of control systems. *IFAC Proceedings Volumes*, 1(1):491–502, aug 1960.

[23] Andre Kayser. Übertragung vom batch zu einer kontinuierlichen produktion: Experimentelle untersuchung einer kontinuierlichen copolymerisation in einem wendelrohrreaktor. Master's thesis, TU Dortund University, 2017.

[24] Hassan K. Khalil. *Nonlinear Systems*. Prentice Hall, 1995.

[25] Stephan Klutz, Safa Kutup Kurt, Martin Lobedann, and Norbert Kockmann. Narrow residence time distribution in tubular reactor concept for reynolds number range of 10–100. *Chemical Engineering Research and Design*, 95:22–33, mar 2015.

[26] Ande Küsters. Übertragung vom batch zu einer kontinuierlichen produktion: Modulares konzept einer rohrreaktoranlage für copolymerisationen. Master's thesis, TU Dortund University, 2016.

[27] Jingyu Liu. Evaluation of state and parameter estimation methods for a polymerization test case in the do-mpc framework. Master's thesis, TU Dortmund University, 2018.

[28] Sergio Lucia, Alexandru Tătulea-Codrean, Christian Schoppmeyer, and Sebastian Engell. Rapid development of modular and sustainable nonlinear model predictive control solutions. *Control Engineering Practice*, 60:51–62, mar 2017.

[29] R. Mahalingam, L.O. Tilton, and J.M. Coulson. Heat transfer in laminar flow of non-newtonian fluids. *Chemical Engineering Science*, 30(8):921–929, aug 1975.

[30] D. S. Malkus, W. G. Pritchard, and M. Yao. The hole-pressure effect and viscometry. *Rheologica Acta*, 31(6):521–534, 1992.

[31] M. Mansour, Z. Liu, G. Janiga, K.D.P. Nigam, K. Sundmacher, D. Thévenin, and K. Zähringer. Numerical study of liquid-liquid mixing in helical pipes. *Chemical Engineering Science*, 172:250–261, nov 2017.

[32] Erlita Mastan and Shiping Zhu. Method of moments: A versatile tool for deterministic modeling of polymerization kinetics. *European Polymer Journal*, 68:139–160, jul 2015.

[33] George Odian. *Principles of Polymerization*. John Wiley & Sons, Inc., jan 2004.

[34] Katsuhiko Ogata. *Discrete-Time Control Systems (2nd Edition)*. Pearson, 1995.

[35] C. Paige. Properties of numerical algorithms related to computing controllability. *IEEE Transactions on Automatic Control*, 26(1):130–138, feb 1981.

[36] James B. Rawlings and Mayne David Q. *Model Predictive Control Theory and Design*. Nob Hill Pub, Llc, 2009.

[37] Patrick Rojahn, Volker Hessel, Krishna D.P. Nigam, and Frank Schael. Applicability of the axial dispersion model to coiled flow inverters containing single liquid phase and segmented liquid-liquid flows. *Chemical Engineering Science*, 182:77–92, jun 2018.

[38] Damiano Rossi, Luigi Gargiulo, Gleb Valitov, Asterios Gavriilidis, and Luca Mazzei. Experimental characterization of axial dispersion in coiled flow inverters. *Chemical Engineering Research and Design*, 120:159–170, apr 2017.

[39] Michael Rubinstein. *Polymer Physics*. OUP Oxford, 2003.

[40] A. K. Saxena and K. D. P. Nigam. Coiled configuration for flow inversion and its effect on residence time distribution. *AIChE Journal*, 30(3):363–368, may 1984.

[41] René Schneider and Christos Georgakis. How to NOT make the extended kalman filter fail. *Industrial & Engineering Chemistry Research*, 52(9):3354–3362, feb 2013.

[42] Robin Lukas Semrau. Validation of an output-feedback nmpc scheme for a cfi polymerization reactor. Master's thesis, Technische Universität Dortmund, 2019.

[43] Ian Postlethwaite Sigurd Skogestad. *Multivariable Feedback Control*. John Wiley & Sons, 2005.

[44] Dan Simon. *Optimal State Estimation*. John Wiley & Sons, Inc., jan 2006.

[45] Fischer Mess und Regeltechnik. De40 - differential pressure transmitter. Product operating manual, 2019.

[46] Jaleel Valappil and Christos Georgakis. Systematic estimation of state noise statistics for extended kalman filters. *AIChE Journal*, 46(2):292–308, feb 2000.

[47] M. Verhaegen and P. Van Dooren. Numerical aspects of different kalman filter implementations. *IEEE Transactions on Automatic Control*, 31(10):907–917, oct 1986.

[48] Niklas Wahlström, Patrix Axelsson, and Fredrik Gustafsson. Discretizing stochastic dynamical systems using lyapunov equations. *IFAC Proceedings Volumes*, 47(3):3726–3731, 2014.

[49] Jiayan Xu. Implementation and design of a mpc scheme for a copolymerization process. Master's thesis, TU Dortmund University, 2018.

[50] Haizheng Zhang. Constrained extended kalman filter: an efficient improvement of calibration for dynamic traffic assignment models. Master's thesis, Massachusetts Institute of Technology, 2016.

Appendix A

Additional topics in modelling

A.1 Expressions for the reaction rates

Initiator, radical and inhibitor

$$r_{\mathrm{Ini}} = -k_d \cdot c_{\mathrm{Ini}} \tag{A.1.1}$$

$$r_{\mathrm{R}^\bullet} = 2 \cdot k_d \cdot f \cdot c_{\mathrm{Ini}} - k_{i,1} \cdot c_{\mathrm{R}^\bullet} \cdot c_{\mathrm{M}_1} - k_{i,2} \cdot c_{\mathrm{R}^\bullet} \cdot c_{\mathrm{M}_2} - k_{inh} \cdot c_{\mathrm{R}^\bullet} \cdot c_{\mathrm{O}_2} \tag{A.1.2}$$

$$r_{\mathrm{O}_2} = -k_{inh} \cdot c_{\mathrm{O}_2} \cdot (c_{\mathrm{R}^\bullet} + P_{1,0} + P_{2,0}) \tag{A.1.3}$$

Monomers

$$r_{\mathrm{M}_1} = -k_{i,1} \cdot c_{\mathrm{R}^\bullet} \cdot c_{\mathrm{M}_1} - k_{p,11} \cdot c_{\mathrm{M}_1} \cdot P_{1,0} - k_{p,21} \cdot P_{2,0} \cdot c_{\mathrm{M}_1} \tag{A.1.4}$$

$$r_{\mathrm{M}_2} = -k_{i,2} \cdot c_{\mathrm{R}^\bullet} \cdot c_{\mathrm{M}_2} - k_{p,22} \cdot c_{\mathrm{M}_2} \cdot P_{2,0} - k_{p,12} \cdot P_{1,0} \cdot c_{\mathrm{M}_2} \tag{A.1.5}$$

First monomer active chain

$$\begin{aligned} r_{P_{1,0}} = \quad & -k_{inh} \cdot P_{1,0} \cdot c_{\mathrm{O}_2} + k_{i,1} \cdot c_{\mathrm{R}\bullet} \cdot c_{\mathrm{M}_1} - k_{p,12} \cdot P_{1,0} \cdot c_{\mathrm{M}_2} \\ & + k_{p,21} \cdot P_{2,0} \cdot c_{\mathrm{M}_1} - k_{tc,1} \cdot P_{1,0}^2 - k_{td,1} \cdot P_{1,0}^2 \\ & - k_{tc,12} \cdot P_{2,0} \cdot P_{1,0} - k_{td,12} \cdot P_{2,0} \cdot P_{1,0} \end{aligned} \tag{A.1.6}$$

$$\begin{aligned} r_{P_{1,1}} = \quad & -k_{inh} \cdot P_{1,1} \cdot c_{\mathrm{O}_2} + k_{i,1} \cdot c_{\mathrm{R}\bullet} \cdot c_{\mathrm{M}_1} + k_{p,11} \cdot c_{\mathrm{M}_1} \cdot P_{1,0} \\ & - k_{p,12} \cdot P_{1,1} \cdot c_{\mathrm{M}_2} + k_{p,21} \cdot (P_{2,0} + P_{2,1}) \cdot c_{\mathrm{M}_1} \\ & - k_{tc,1} \cdot P_{1,0} \cdot P_{1,1} - k_{td,1} \cdot P_{1,0} \cdot P_{1,1} \\ & - k_{tc,12} \cdot P_{1,1} \cdot P_{2,0} - k_{td,12} \cdot P_{1,1} \cdot P_{2,0} \end{aligned} \tag{A.1.7}$$

$$\begin{aligned} r_{P_{1,2}} = \quad & -k_{inh} \cdot P_{1,2} \cdot c_{\mathrm{O}_2} + k_{i,1} \cdot c_{\mathrm{R}\bullet} \cdot c_{\mathrm{M}_1} \\ & + k_{p,11} \cdot c_{\mathrm{M}_1} \cdot (P_{1,0} + 2 \cdot P_{1,1}) - k_{p,12} \cdot P_{1,2} \cdot c_{\mathrm{M}_2} \\ & + k_{p,21} \cdot (P_{2,0} + 2 \cdot P_{2,1} + P_{2,2}) \cdot c_{\mathrm{M}_1} - k_{tc,1} \cdot P_{1,0} \cdot P_{1,2} \\ & - k_{td,1} \cdot P_{1,0} \cdot P_{1,2} - k_{tc,12} \cdot P_{1,2} \cdot P_{2,0} - k_{td,12} \cdot P_{1,2} \cdot P_{2,0} \end{aligned} \tag{A.1.8}$$

Second monomer active chain

$$\begin{aligned} r_{P_{2,0}} = \quad & -k_{inh} \cdot P_{2,0} \cdot c_{\mathrm{O}_2} + k_{i,2} \cdot c_{\mathrm{R}\bullet} \cdot c_{\mathrm{M}_2} + k_{p,12} \cdot P_{1,0} \cdot c_{\mathrm{M}_2} \\ & - k_{p,21} \cdot P_{2,0} \cdot c_{\mathrm{M}_1} - k_{tc,1} \cdot P_{2,0}^2 - k_{td,2} \cdot P_{2,0}^2 \\ & - k_{tc,12} \cdot P_{1,0} \cdot P_{2,0} - k_{td,12} \cdot P_{1,0} \cdot P_{2,0} \end{aligned} \tag{A.1.9}$$

$$\begin{aligned} r_{P_{2,1}} = \quad & -k_{inh} \cdot P_{2,1} \cdot c_{\mathrm{O}_2} + k_{i,2} \cdot c_{\mathrm{R}\bullet} \cdot c_{\mathrm{M}_2} + k_{p,22} \cdot c_{\mathrm{M}_2} \cdot P_{2,0} \\ & + k_{p,12} \cdot (P_{1,0} + P_{1,1}) \cdot c_{\mathrm{M}_2} - k_{p,21} \cdot P_{2,1} \cdot c_{\mathrm{M}_1} \\ & - k_{tc,2} \cdot P_{2,1} \cdot P_{2,1} - k_{td,2} \cdot P_{2,0} \cdot P_{2,1} \\ & - k_{tc,12} \cdot P_{1,0} \cdot P_{2,1} - k_{td,12} \cdot P_{1,0} \cdot P_{2,1} \end{aligned} \tag{A.1.10}$$

$$\begin{aligned} r_{P_{2,2}} = \quad & -k_{inh} \cdot P_{2,2} \cdot c_{\mathrm{O}_2} + k_{i,2} \cdot c_{\mathrm{R}\bullet} \cdot c_{\mathrm{M}_2} \\ & + k_{p,22} \cdot c_{\mathrm{M}_2} \cdot (P_{2,0} + 2 \cdot P_{2,1}) - k_{p,21} \cdot P_{2,2} \cdot c_{\mathrm{M}_1} \\ & + k_{p,12} \cdot (P_{1,0} + 2 \cdot P_{1,1} + P_{1,2}) \cdot c_{\mathrm{M}_2} - k_{tc,2} \cdot P_{2,0} \cdot P_{2,2} \\ & - k_{td,2} \cdot P_{2,0} \cdot P_{2,2} - k_{tc,12} \cdot P_{1,0} \cdot P_{2,2} - k_{td,12} \cdot P_{1,0} \cdot P_{2,2} \end{aligned} \tag{A.1.11}$$

Dead polymer

$$r_{D_0} = k_{inh} \cdot (P_{1,0} + P_{2,0}) \cdot c_{O_2} + (k_{tc,12} + 2 \cdot k_{td,12}) \cdot P_{1,0} \cdot P_{2,0} + (0.5 \cdot k_{tc,1} + k_{td,1}) \cdot P_{1,0}^2 + (0.5 \cdot k_{tc,2} + k_{td,2}) \cdot P_{2,0}^2 \tag{A.1.12}$$

$$r_{D_1} = k_{inh} \cdot (P_{1,1} + P_{2,1}) \cdot c_{O_2} + (k_{tc,12} + k_{td,12}) \cdot (P_{1,0} \cdot P_{2,1} + P_{1,1} \cdot P_{2,0}) + (k_{tc,1} + k_{td,1}) \cdot P_{1,0} \cdot P_{1,1} + (k_{tc,2} + k_{td,2}) \cdot (P_{2,0} \cdot P_{2,1}) \tag{A.1.13}$$

$$r_{D_2} = k_{inh} \cdot (P_{1,2} + P_{2,2}) \cdot c_{O_2} + k_{td,1} \cdot P_{1,0} \cdot P_{1,2} + k_{td,2} \cdot P_{2,0} \cdot P_{2,2} + k_{tc,1} \cdot (P_{1,0} \cdot P_{1,2} + P_{1,1}^2) + k_{tc,2} \cdot (P_{2,0} \cdot P_{2,2} + P_{2,1}^2) + k_{tc,12} \cdot (P_{1,0} \cdot P_{2,2} + 2 \cdot P_{1,1} \cdot P_{2,1} + P_{1,2} \cdot P_{2,0}) + k_{td,12} \cdot (P_{1,2} \cdot P_{2,0} + P_{2,2} \cdot P_{1,0}) \tag{A.1.14}$$

A.2 Correlations for axial dispersion in the CFI reactor

The axial dispersion coefficient is correlated to the flow conditions, the geometry and the properties of the fluid through the dimensionless numbers:

$$Re = \frac{\rho \cdot v \cdot d_{in}}{\eta} \tag{A.2.1}$$

$$Sc = \frac{\eta}{\mathcal{D} \cdot \rho} \tag{A.2.2}$$

$$Bo = \frac{v \cdot L}{D_{ax}} \tag{A.2.3}$$

Where $\mathcal{D}$ is the molar diffusivity of the component under consideration. The viscosity used for computing Sc and Re is Newtonian, was determined in [9] and is modelled as a function of the polymer mass fraction ω:

$$\eta - \eta_{water} = 17.6607 \cdot \omega^2 \ (Pa \cdot s) \tag{A.2.4}$$

The weight fraction of the polymer can be approximated by defining two additional state variables (co_{M_1} and co_{M_2}), which derivatives are respectively:

$$\frac{\partial co_{\mathrm{M}_1}}{\partial t} = -\frac{\partial c_{\mathrm{M}_1}}{\partial t} \tag{A.2.5}$$

$$\frac{\partial co_{\mathrm{M}_2}}{\partial t} = -\frac{\partial c_{\mathrm{M}_2}}{\partial t} \tag{A.2.6}$$

The total mass of the polymer can be approximated by the mass of the reacted monomers, with the knowledge about the molar masses, therefore:

$$\omega = \frac{M_{\mathrm{M}_1} co_{\mathrm{M}_1} + M_{\mathrm{M}_1} co_{\mathrm{M}_1}}{\rho} \tag{A.2.7}$$

The density of the mixture ρ is assumed to be constant.

Correlations for Bo are available in literature [38, 40, 37] for different geometries and flow conditions. The correlation used in this work was assembled from those sources:

$$Bo = \frac{L}{d_{in}} \left[\left(\frac{n_{bend} + 1}{20} \right)^{0.58} \cdot \left(\frac{Sc}{192} \cdot k1 \cdot Re^{k2} \right)^{-1} + \left(\frac{1}{Sc \cdot Re} + \frac{Sc \cdot Re}{192} \right)^{-1} \right] \tag{A.2.8}$$

A.3 Correlations for heat transfer in the CFI reactor

The heat transfer coefficients are expressed as functions of the Reynolds number Re, the Prandtl number Pr and the Nusselt number Nu:

$$Pr = \frac{\eta \cdot C_P}{\lambda} \tag{A.3.1}$$

$$Nu = \frac{h \cdot d_{in}}{\lambda} \tag{A.3.2}$$

The correlation for the Nusselt number in coiled flow applications was taken from [14]:

$$Nu = 3.66 + 0.08 \cdot \left[1 + 0.8 \cdot \left(\frac{d_{in}}{d_D}\right)^{0.9}\right] \cdot Re^m \cdot Pr^{1/3} \tag{A.3.3}$$

$$UA_2 = \left(\frac{1}{h \cdot A_i} + \frac{\log(d_o/d_i)}{\lambda_t \cdot 2 \cdot \pi}\right)^{-1} \tag{A.3.4}$$

A.4 State variables

The state of the system can be visualized a 18×15 matrix that is then unfolded in a 270×1 vector for numerical computations. The relationship between the state matrix and the state vector is as follows:

$$x = \begin{pmatrix} X_1 \\ X_2 \\ \vdots \\ X_{15} \end{pmatrix} \tag{A.4.1}$$

with X_j the $j-$th column of the X matrix.

The elements of X_j are described in table A.1.

Element	State	Units	Description
$X_{j,1}$	c_{Ini}	mol/m^3	Concentration of initiator
$X_{j,2}$	$c_{\mathrm{R}\bullet}$	mol/m^3	Concentration of the active radical
$X_{j,3}$	c_{M_1}	mol/m^3	Concentration of acrylamide
$X_{j,4}$	P_{10}	mol/m^3	Zeroth moment of the acrylamide active polymer chain
$X_{j,5}$	P_{11}	mol/m^3	First moment of the acrylamide active polymer chain
$X_{j,6}$	P_{12}	mol/m^3	Second moment of the acrylamide active polymer chain
$X_{j,7}$	c_{M2}	mol/m^3	Concentration of AMPS
$X_{j,8}$	P_{20}	mol/m^3	Zeroth moment of the AMPS active polymer chain
$X_{j,9}$	P_{21}	mol/m^3	First moment of the AMPS active polymer chain
$X_{j,10}$	P_{22}	mol/m^3	Second moment of the AMPS active polymer chain
$X_{j,11}$	D_0	mol/m^3	Zeroth moment of the dead polymer chain
$X_{j,12}$	D_1	mol/m^3	First moment of the dead polymer chain
$X_{j,13}$	D_2	mol/m^3	Second moment of the dead polymer chain
$X_{j,14}$	T_t	K	Tube temperature
$X_{j,15}$	T_r	K	Reaction medium temperature
$X_{j,16}$	c_{O_2}	mol/m^3	Concentration of inhibitor/oxygen
$X_{j,17}$	$\mathrm{co}_{\mathrm{M}_1}$	mol/m^3	Concentration tracking state of acrylamide consumption
$X_{j,18}$	$\mathrm{co}_{\mathrm{M}_2}$	mol/m^3	Concentration tracking state of AMPS consumption

Table A.1: State variables per grid point

Appendix B

Process flow diagram of the plant

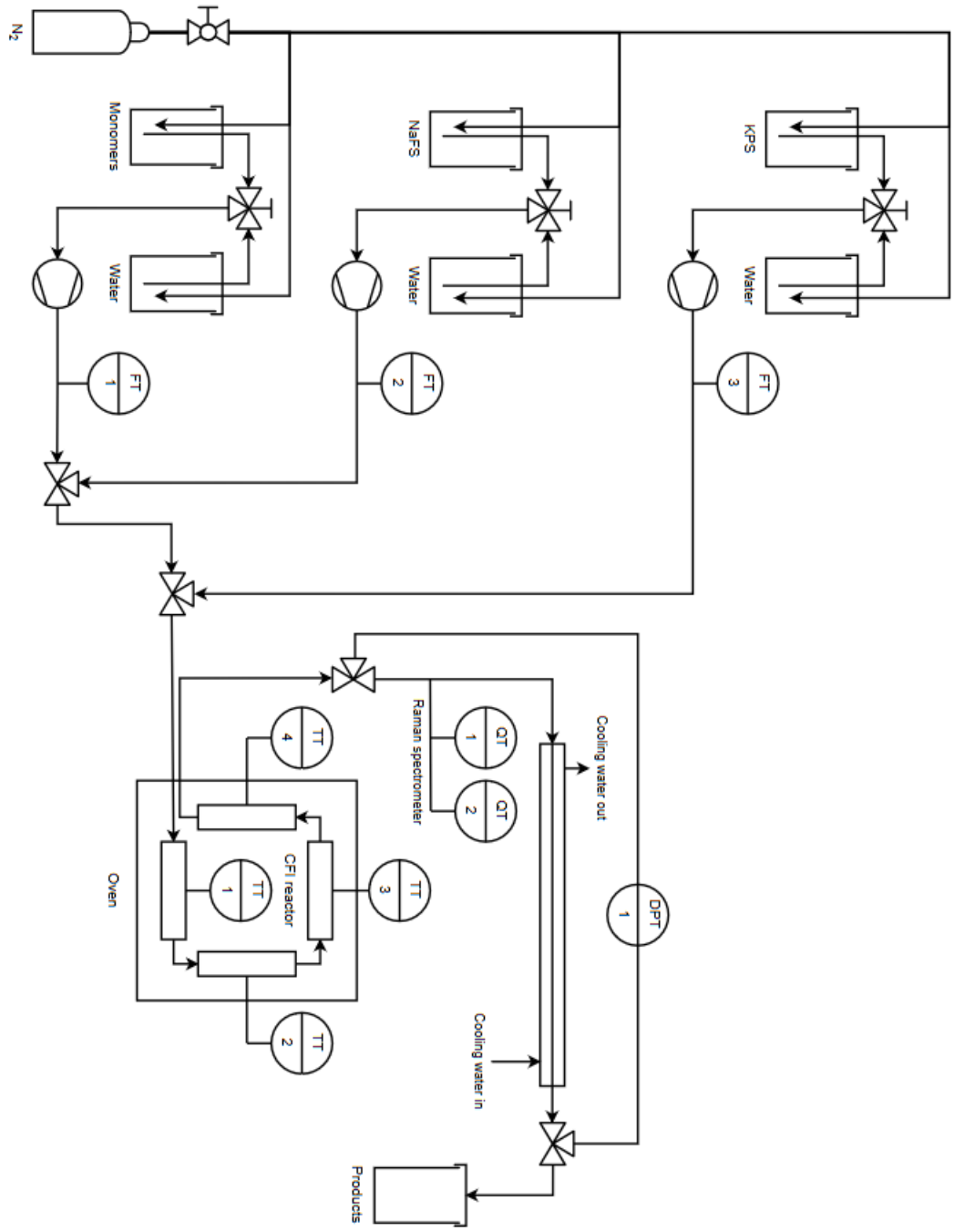

Figure B.1: Process flow diagram of the plant

Appendix C

Linear algebra topics

C.1 Singular value decomposition

The singular value decomposition (SVD) of a matrix $A \in \mathbb{R}^{m \times n}$ is the matrix factorization defined as [18]:

$$A = U \Sigma V^T \tag{C.1.1}$$

where $U = (u_1, u_2, \ldots, u_r, u_{r+1}, \ldots, u_m) \in \mathbb{R}^{m \times m}$ and $V = (v_1, v_2, \ldots, v_n) \in \mathbb{R}^{n \times n}$ are orthogonal matrices and $\Sigma = \begin{pmatrix} \operatorname{diag}(\sigma_1, \sigma_2, \ldots, \sigma_r, 0, \ldots, 0) \\ 0 \end{pmatrix} \in \mathbb{R}^{m \times n}$

The elements $\sigma_1 \geq \sigma_2 \geq \cdots \geq \sigma_r$ are called singular values.

C.2 Moore-Penrose inverse

The Moore-Penrose inverse A^+ of a matrix A is a generalization of the matrix inverse for rank-deficient or non-square matrices that satisfies the four Moore-Penrose conditions [6]:

$$AA^+A = A \tag{C.2.1}$$

$$A^+AA^+ = A^+ \tag{C.2.2}$$

$$(AA^+)^T = AA^+ \tag{C.2.3}$$

$$(A^+A)^T = A^+A \tag{C.2.4}$$

If $A = U\Sigma V^T$is the singular value decomposition of A, it is possible to compute the Moore-Penrose inverse as [18]:

$$A^+ = \sum_{i=1}^{r} \frac{v_i u_i^T}{\sigma_i} \tag{C.2.5}$$

Usually the summation is truncated to some σ_p smaller than a tolerance.

C.3 Matrix exponential

The matrix exponential of a square matrix A is defined as the power series

$$e^A = \sum_{k=0}^{\infty} \frac{1}{k!} A^k \tag{C.3.1}$$

It is computed in numerical packages using specialized algorithms such as the scaling and squaring algorithm [20].

List of Tables

List of Figures

List of Algorithms